

Magnetic fields in the multiphase interstellar medium of the Milky Way: turbulent kinetic and magnetic energy density relation

Amit Seta^{*} and N. M. McClure-Griffiths

Research School of Astronomy and Astrophysics, Australian National University, Canberra, ACT 2611, Australia

Accepted XXX. Received YYY; in original form ZZZ

ABSTRACT

Magnetic fields are an important component of the interstellar medium (ISM) of galaxies. The thermal gas in the ISM has a multiphase structure, broadly divided into ionised, atomic, and molecular phases. The connection between the multiphase ISM gas and magnetic field is not known and this makes it difficult to account for their impact on star formation and galaxy evolution. Usually, in star formation studies, a relationship between the gas density, n and magnetic field strength, B , is assumed to study magnetic fields' impact. However, this requires the knowledge of the geometry of star-forming regions and ambient magnetic field orientation. Here, we use the Zeeman magnetic field measurements from the literature for the atomic and molecular ISM and supplement the magnetic field estimates in the ionised ISM using pulsar observations to find a relation between the turbulent kinetic, E_{kin} , and magnetic, E_{mag} , energy densities. Across all three phases and over a large range of densities ($10^{-3} \text{ cm}^{-3} \lesssim n \lesssim 10^7 \text{ cm}^{-3}$), we find $E_{\text{mag}} \propto E_{\text{kin}}$. Furthermore, we use phase-wise probability density functions of density, magnetic fields, and turbulent velocities to show that the magnetic field fluctuations are controlled by both density and turbulent velocity fluctuations. This work demonstrates that a combination of both the density and turbulent velocity determines magnetic fields in the ISM.

Key words: magnetic fields – turbulence – ISM: magnetic fields – galaxies: magnetic fields – methods: observational – methods: statistical

1 INTRODUCTION

The interstellar medium (ISM) of star-forming galaxies is a dynamic medium between stars consisting of thermal gas, dust, radiation, turbulence, magnetic fields, and cosmic rays. Magnetic fields are an energetically important component of the ISM as they play a crucial role in star formation (Mestel & Spitzer 1956; Krumholz & Federath 2019; Pattle et al. 2023), propagation of cosmic rays (Cesarsky 1980; Zweibel 2017; Ruszkowski & Pfrommer 2023), determining properties of galactic outflows (Veilleux et al. 2005; van de Voort et al. 2021; Thompson & Heckman 2024), and might also play a significant role in the evolution of galaxies (Naab & Ostriker 2017; Martin-Alvarez et al. 2020; Pakmor et al. 2024). Despite their significance, the ISM's thermal gas-magnetic field connection is poorly understood. This makes it difficult to study the role of magnetic fields in star formation and galaxy evolution – two outstanding problems in modern astrophysics.

The matter and energy in galaxies cycles between the stars and the ISM. Stars are continuously formed from the cold, dense, molecular ISM, where the self-gravity of gas leads to a collapse. Then the stars through stellar outflows and, primarily for massive stars, supernova explosions, return energy and material back into the ISM generating turbulence and the hot, ionised ISM gas. The hot, ionised gas cools (Sutherland & Dopita 1993) to form the warm, atomic ISM. The atoms combine to form molecules creating the molecular ISM, which

again could potentially form stars. Thus, the gas in galaxies cycles through these multiple phases and in a dynamic equilibrium state, it gives rise to a multiphase structure (Field et al. 1969; McKee & Ostriker 1977; Cox 2005). More generally, the ISM gas can be in various forms: molecular (cold), atomic (cold and warm), and ionised (warm and hot) phases (also see Dickey & Lockman 1990; Wolfire et al. 1995, 2003; Kalberla & Kerp 2009; Ferrière 2020; Saintonge & Catinella 2022; McClure-Griffiths et al. 2023). The properties of several ISM components, most notably, turbulence, magnetic fields, and cosmic rays vary with the ISM phase. In this work, we primarily study the multiphase gas-magnetic field connection.

Between the ISM phases (ionised, atomic, and molecular), the gas number density, n , varies over a huge range, from 10^{-3} cm^{-3} in the ionised ISM to up to 10^7 cm^{-3} in the molecular ISM (see Table 1 in Ferrière 2020). In collapsing molecular clouds, magnetic fields amplify due to compression. A relationship between n and magnetic field strength, B , is usually assumed in such a scenario to determine the dynamical importance of magnetic fields on the formation of stars. For example, in the case of isotropic spherical collapse, $B \propto n^{2/3}$ (Mestel 1966) and for collapse parallel to the magnetic field, $B \propto n^{1/2}$ (Mouschovias 1976a,b). Generally, depending on the geometry of the collapsing cloud and the orientation of the magnetic field relative to the collapsing direction, the $B - n$ relation could vary (see Fig. 1 in Trites et al. 2015). Using Zeeman measurements of magnetic field strengths in the atomic (HI) and molecular (OH and CN) ISM, Crutcher et al. (2010) showed that $B - n$ relation is a broken power-law function with $B \propto n^0$ below the critical density

* E-mail: amit.seta@anu.edu.au

$n_{\text{crit}} \approx 300 \text{ cm}^{-3}$ and $B \propto n^{2/3}$ above that. [Tritsis et al. \(2015\)](#) reanalysed the same data and, for the molecular ISM, concluded $B \propto n^{1/2}$ instead of $B \propto n^{2/3}$. Including magnetic fields in the ionised phase of HII regions with these Zeeman measurements, [Harvey-Smith et al. \(2011\)](#) found $B \propto n^{0.11}$ below $n_{\text{crit}} \approx 480 \text{ cm}^{-3}$ and $B \propto n^{0.66}$ for densities above it. Using far-infrared and HI data, [Kalberla & Haud \(2023\)](#) found $B \propto n^{0.58}$ for $0.1 \text{ cm}^{-3} \lesssim n \lesssim 100 \text{ cm}^{-3}$. More recently, [Whitworth et al. \(2024\)](#), combined these Zeeman measurements with magnetic fields from dust polarisation observations ([Pattle et al. 2023](#)) and concluded $B \propto n^{(0.27 \pm 0.017)}$ for $n \leq n_{\text{crit}} \approx 924_{-144}^{+154} \text{ cm}^{-3}$ and $B \propto n^{(0.54 \pm 0.18)}$ for $n > n_{\text{crit}}$. In this paper, besides the atomic and molecular ISM, we also explore magnetic fields in the ionised ISM using pulsar observations.

A variety of magnetohydrodynamic turbulence simulations show a huge scatter around and differences with the expected $B - n$ relations (e.g., see Fig. 5 in [Seta & Federrath 2022](#), Fig. 1 in [Ponnada et al. 2022](#), Fig. 7 in [Hu et al. 2023](#), Fig. 7 in [Konstantinou et al. 2024](#), Fig. 5 – 6 in [He & Ricotti 2024](#), and Fig. 6 – 14 in [Whitworth et al. 2024](#)) demonstrating that, in general, the magnetic field does not necessarily depend only on the gas density. The prevailing ISM turbulence, especially in the ionised and atomic ISM, also further complicates the applicability of the $B - n$ relations (which are largely based on systematic compression or collapse scenarios). Turbulence in the ISM is driven on a range of scales by different processes, from stellar outflows at sub-pc scales to supernova explosions at $\approx 100 \text{ pc}$ ([Mac Low & Klessen 2004](#); [Elmegreen & Scalo 2004](#); [Scalo & Elmegreen 2004](#)) to gravitational instabilities at even larger kpc scales ([Krumholz & Burkhardt 2016](#); [Krumholz et al. 2018](#)). The properties of turbulence also vary with the ISM phase: turbulence is supersonic in the cold (atomic and molecular) ISM and transonic/subsonic in the warm (ionised and atomic) and hot (ionised) ISM ([Larson 1981](#); [Heiles & Troland 2003b](#); [Gaensler et al. 2011](#); [Murray et al. 2015](#); [Nguyen et al. 2019](#); [Marchal & Miville-Deschênes 2021](#); [Federrath et al. 2021](#)). Both the density and turbulent velocity in the ISM phases could be together characterised using the turbulent kinetic energy, $E_{\text{kin}} = 0.5 n \delta v_{\text{turb}}^2$, where δv_{turb} is the turbulent velocity. Using E_{kin} , in this work, we aim to determine a relation that captures the multiphase gas-magnetic field connection better than the existing $B - n$ relations and also factors in the turbulence scenario.

In addition to introducing density and velocity fluctuations, ISM turbulence also affects magnetic field properties. Magnetohydrodynamic turbulence simulations, which start with initially weak magnetic fields, show magnetic field amplification and, once the magnetic field achieves a statistically steady state, the amplified magnetic energy density, $E_{\text{mag}} = B^2/8\pi$, is proportional to E_{kin} (this need not necessarily be the case for simulations that start with dynamically strong fields). This is due to a dynamo process, which is the conversion of turbulent kinetic energy into magnetic energy ([Kazantsev 1968](#); [Zel'dovich et al. 1984](#); [Ruzmaikin et al. 1988](#); [Kulsrud & Anderson 1992](#); [Beck et al. 1996](#); [Brandenburg & Subramanian 2005](#); [Rincon 2019](#); [Shukurov & Subramanian 2021](#); [Schekochihin 2022](#)). The dynamo amplifies weak seed magnetic fields in protogalaxies and the early Universe ($\sim 10^{-10} \mu\text{G}$; see [Kulsrud et al. 1997](#); [Subramanian 2016](#); [Seta & Federrath 2020](#)) to roughly equipartition field strengths (i.e., $E_{\text{mag}} \approx E_{\text{kin}}$, $\sim 1 - 10 \mu\text{G}$) and maintains it against decay and dissipation. The equipartition field strengths are also observed in present-day ([Beck 2016](#)) and relatively young ([Bernet et al. 2008](#); [Mao et al. 2017](#); [Seta et al. 2021](#); [Shah & Seta 2021](#); [Mahony et al. 2022](#)) galaxies. This process has been extensively studied using a variety of numerical simulations ([Meneguzzi et al. 1981](#); [Schekochihin et al. 2004](#); [Haugen et al. 2004](#); [Federrath et al. 2011](#); [Schober et al. 2012](#); [Gent et al. 2013](#); [Federrath et al. 2014](#); [Federrath](#)

[2016](#); [Rieder & Teyssier 2017](#); [Seta et al. 2020](#); [Seta & Federrath 2021a](#); [Achikanath Chirakkara et al. 2021](#); [Seta & Federrath 2022](#); [Gent et al. 2023](#); [Brandenburg & Ntormousi 2023](#); [Sur & Subramanian 2024](#); [Korpi-Lagg et al. 2024](#)). For all of these simulations, in the statistically steady state, $E_{\text{mag}} \propto E_{\text{kin}}$. Although the level of energy equipartition ($E_{\text{mag}}/E_{\text{kin}}$) may depend on the ISM phase ($E_{\text{mag}}/E_{\text{kin}}$ is roughly an order of magnitude higher in the warm phase in comparison to the cold phase, see [Seta & Federrath 2022](#), for further details). In this paper, using multiple Milky Way observations, we show that $E_{\text{mag}} \propto E_{\text{kin}}$ holds across several ISM phases over a large range of densities and is a physically more concrete alternative to the popular $B - n$ relations.

The paper is organised as follows. In Sec. 2, we present the observational datasets and methods used to derive E_{mag} and E_{kin} . The $E_{\text{mag}} - E_{\text{kin}}$ relation is discussed in Sec. 3. In Sec. 4, we further discuss the assumptions in and impact of the derived $E_{\text{mag}} - E_{\text{kin}}$ relation. Finally, we summarise and conclude our work in Sec. 5.

2 DATA AND METHOD

In this paper, we seek to compare data that probe the magnetic field energy density, E_{mag} , and the kinetic energy density, E_{kin} , across molecular, atomic, and ionised gas phases. To do this, we compile observations of the Zeeman effect in atomic and molecular gas, which give localised measurements of the line-of-sight magnetic field strength and turbulent velocity widths, along with estimates of the gas density. We augment these with estimates of the mean line-of-sight gas density and magnetic field strength from pulsar observations, combined with estimates of the turbulent velocity from both ionised and atomic gas tracers. Inherent in our analysis is the assumption that when considering population-based statistics, the line-of-sight mean properties for ionised gas can be compared with localised measurements, like those from Zeeman (further discussed in Sec. 4.1). In this section, we describe the data sources and our method, in Sec. 3, we present our results, and in Sec. 4, we justify the validity of the assumptions that are inherent in comparing these different types of data.

2.1 Zeeman data for the atomic and molecular ISM

The Zeeman data for both the atomic (HI) and molecular (OH and CN) ISM is taken from Table 1 in [Crutcher et al. \(2010\)](#). This includes the line-of-sight magnetic fields, B_{los} , the estimated uncertainty in B_{los} , $B_{\text{los, err}}$, and the gas density, n , for 137 sources. We divide the entire data set into two subsets: one which probes the atomic ISM (referred to as the Zeeman, HI dataset) and the other which probes the molecular ISM (referred to as the Zeeman, Mol dataset).

The velocity widths, δv , are also obtained differently for Zeeman, HI and Zeeman, Mol datasets. For the atomic ISM, the Stokes I spectrum (total intensity vs. velocity) of the HI line is fitted with Gaussian distributions ([Heiles & Troland 2003a](#)) to determine the magnetic field strength (e.g. see Sec. 2.8 in [Heiles & Troland 2004](#)), which gives the velocity line widths, δv , and associated uncertainties, δv_{err} , from the fitting. The δv and δv_{err} corresponding to the sources in the Zeeman, HI dataset are taken from Table 1 in [Heiles & Troland \(2004\)](#). For the molecular ISM, the numerical derivative of the Stokes I spectrum is fitted to the Stokes V (circular polarisation) spectrum to obtain the magnetic field strength (e.g. see Eq. 3 in [Crutcher & Kemball 2019](#)) and δv s are known. For the Zeeman, Mol dataset, the corresponding δv s are taken from the literature ([Crutcher 1999](#); [Troland & Crutcher 2008](#); [Falgarone et al.](#)

2008, and references there in) and, for each source, the δv_{err} is taken to be 5% of their corresponding line-width, δv (Crutcher, Richard M., private communication).

After compiling the data ($n, B_{\text{los}}, B_{\text{los, err}}, \delta v, \delta v_{\text{err}}$) for all of the 137 sources in Table 1 of Crutcher et al. (2010), we discard sources with $B_{\text{los}} = 0$ (one component of the source 3C 348 in the Zeeman, HI dataset) and $\delta v_{\text{err}} = 0$ (one component of two sources, 3C 225b and 3C 237, in the Zeeman, HI dataset). This leaves us with a total of 134 sources in our sample, 66 in the Zeeman, HI dataset and 68 in the Zeeman, Mol dataset.

2.2 Pulsar data for the ionised ISM

We use pulsar observations to probe the gas (thermal electron) number density and magnetic fields in the ionised ISM. Due to the thermal electron density, n_e , along the path between the pulsar and us, the pulsed signals are delayed to lower frequencies and the observed dispersion in the pulse is quantified in terms of the dispersion measure, DM, given by

$$\frac{\text{DM}}{\text{pc cm}^{-3}} = \int_{L_{\text{pul}}/\text{pc}} \frac{n_e}{\text{cm}^{-3}} d\left(\frac{l}{\text{pc}}\right), \quad (1)$$

where L_{pul} is the distance from the pulsar to us. Also, the linearly polarised emission from the pulsar undergoes Faraday rotation due to n_e and line-of-sight magnetic fields, B_{los} , along the path, which is the rotation of the polarisation plane as a function of the observing wavelength, λ , as $\delta\psi = \text{RM} \lambda^2$, where $\delta\psi$ is the change in polarisation angle between the source and observer and RM is the rotation measure, given by

$$\frac{\text{RM}}{\text{rad m}^{-2}} = 0.812 \int_{L_{\text{pul}}/\text{pc}} \frac{n_e}{\text{cm}^{-3}} \frac{B_{\text{los}}}{\mu\text{G}} d\left(\frac{l}{\text{pc}}\right). \quad (2)$$

Knowing the distance to the pulsar, L_{pul} , the average thermal electron density, $\langle n_e \rangle$, can be estimated from the observed DM as

$$\frac{\langle n_e \rangle}{\text{cm}^{-3}} = \frac{\text{DM}}{\text{pc cm}^{-3}} \left(\frac{L_{\text{pul}}}{\text{pc}}\right)^{-1}. \quad (3)$$

Furthermore, from RM (Eq. 2) and DM (Eq. 1), the average B_{los} can be obtained as

$$\frac{\langle B_{\text{los}} \rangle}{\mu\text{G}} = 1.232 \frac{\text{RM}}{\text{rad m}^{-2}} \left(\frac{\text{DM}}{\text{pc cm}^{-3}}\right)^{-1}. \quad (4)$$

Both the derived quantities (Eq. 3 and Eq. 4) from RM and DM observations have been extensively used to study the properties of the ionised ISM and Galactic magnetic fields (Smith 1968; Hewish et al. 1968; Manchester 1972, 1974; Lyne & Smith 1989; Rand & Kulkarni 1989; Han & Qiao 1994; Han et al. 1999; Indrani & Deshpande 1999; Mitra et al. 2003; Berkhuijsen et al. 2006; Han et al. 2004, 2006; Berkhuijsen & Fletcher 2008; Gaensler et al. 2008; Han et al. 2018; Yao et al. 2017; Sobey et al. 2019; Lee et al. 2024). Note that using Eq. 4 to estimate the average line-of-sight magnetic field assumes that the thermal electron density and magnetic fields are uncorrelated (Beck et al. 2003) and this assumption holds for larger \approx kpc distances to pulsars (Seta & Federrath 2021b).

We use RM and DM observations from the ATNF pulsar catalogue (Manchester et al. 2005, <https://www.atnf.csiro.au/research/pulsar/psrcat>, version 2.4.0) for pulsars with only independently determined distances (Dist_A in the catalogue, referred to as L_{pul} , 271 pulsars in total). From this dataset, we remove pulsars with $\text{RM} = 0$, the error in RM, $\text{RM}_{\text{err}} = 0$, $\text{DM} = 0$, and the error in DM, $\text{DM}_{\text{err}} = 0$. This leaves

us with 237 pulsars. Additionally, we choose pulsars with distances, $L_{\text{pul}} \leq 10$ kpc, which further reduces the dataset to 212 pulsars. From this dataset, we compute $\langle n_e \rangle$ and $\langle B_{\text{los}} \rangle$ using Eq. 3 and Eq. 4, respectively. For the ionised ISM, as probed by the pulsar sample, we assume the gas with $n \approx \langle n_e \rangle$ hosts $B_{\text{los}} \approx \langle B_{\text{los}} \rangle$ (this assumption is thoroughly discussed in Sec. 4.1).

2.3 Velocity widths for the ionised ISM, $\delta v_{\text{H}\alpha}$ and δv_{HI}

The pulsar DM and RM measurements do not have any inherent mechanism for estimating the velocity width. To compute velocity widths for the ionised ISM probed by the pulsars, we use spectral lines tracing both the ionised ($\text{H}\alpha$) and atomic (HI) hydrogen along pulsar sight lines. The $\text{H}\alpha$ spectra for pulsar locations are sourced from the Wisconsin $\text{H}\alpha$ Mapper Sky Survey (WHAM survey, Haffner et al. 2003, 2010, <https://www.astro.wisc.edu/research/research-areas/galactic-astronomy/wham/wham-sky-survey>) and has an angular and spectral resolution of 1 deg and 12 km s^{-1} , respectively. The HI emission spectra (data sourced from https://www.astro.uni-bonn.de/hisurvey/AllSky_gauss), depending on the location of the pulsar, are either taken from the Effelsberg - Bonn HI Survey (EBHIS, Winkel et al. 2016) or Parkes Galactic All-Sky Survey (GASS, McClure-Griffiths et al. 2009; Kalberla et al. 2010). The EBHIS dataset has an angular and spectrum resolution of 10.8 arcmin and 1.29 km s^{-1} , respectively, and the GASS dataset has those as 16.2 arcmin and 0.82 km s^{-1} . The HI spectra have a significantly better resolution, especially spectral resolution, than the $\text{H}\alpha$ dataset.

From the $\text{H}\alpha$ and HI data along pulsar sightlines for the Milky Way (local standard of rest velocities within $\pm 50 \text{ km s}^{-1}$, see Sec. 4.3 for a discussion on this choice), we estimate the velocity widths, δv , by computing the square root of the second moment of the spectral line, m_2 , as

$$\delta v = m_2^{1/2} = \left(\frac{\sum_{i=1}^{n_{\text{chan}}} \text{amp}_i (v_i - m_1)^2}{\sum_{i=1}^{n_{\text{chan}}} \text{amp}_i} \right)^{1/2}, \quad (5)$$

where n_{chan} is the number of velocity channels, v_i is the velocity in each channel, amp_i is the amplitude of the line in each channel (in Rayleighs, R, for the $\text{H}\alpha$ spectra and in Kelvin, K, for the HI spectra), and $m_1 = \sum_{i=1}^{n_{\text{chan}}} \text{amp}_i v_i / \sum_{i=1}^{n_{\text{chan}}} \text{amp}_i$ is the first moment. For this computation, the spectra are thresholded at three times the noise level to avoid contributions from spurious peaks (especially at higher velocities), which is a location-dependent quantity in the WHAM survey for the $\text{H}\alpha$ spectra (average level of 0.15 R, see Haffner et al. 2003) and $\approx 100 \text{ mK}$ for the HI spectra (see Table 1 in HI4PI Collaboration et al. 2016). Representative $\text{H}\alpha$ and HI spectra, along with the computed m_1 and m_2 , are shown in Fig. A1 and further discussed in Appendix A. For both the $\text{H}\alpha$ and HI datasets, the error in δv , δv_{err} , is estimated via a Monte Carlo-type method. Random velocities are drawn from each channel (keeping channel width the same) for random amplitudes taken from the range (measurement \pm three times the observed noise level) 5000 times to compute a distribution of δv for each pulsar sightline using Eq. 5. The difference between 84th and 16th percentile of this distribution is taken as δv_{err} .

2.4 Construction of δv_{turb} from δv

Once the velocity widths for the pulsars (both $\delta v_{\text{H}\alpha}$ and δv_{HI}), Zeeman, HI, and Zeeman, Mol datasets are known, we need to estimate the turbulent velocity, δv_{turb} , by removing the contribution from the thermal speed, δv_{ther} . Knowing the Mach number of the

turbulence ($\mathcal{M} = \delta v_{\text{turb}}/\delta v_{\text{ther}}$) and $\delta v = (\delta v_{\text{ther}}^2 + \delta v_{\text{turb}}^2)^{1/2}$, we get

$$\delta v_{\text{turb}} = \delta v \left(\frac{1}{\mathcal{M}^2} + 1 \right)^{-1/2}. \quad (6)$$

Based on the literature, we assume that the Mach number in the ionised ISM, $\mathcal{M}_{\text{ion}} \approx 1$, for both the H α (Hill et al. 2008; Gaensler et al. 2011) and HI (Heiles & Troland 2003b; Marchal & Miville-Deschênes 2021, also, see a discussion in Sec. 4.3 about Mach numbers in the atomic ISM from HI spectra) datasets. In the atomic ISM, $\mathcal{M}_{\text{atm}} \approx 1$, for the Zeeman, HI dataset (Heiles & Troland 2003b; Marchal & Miville-Deschênes 2021) and in the molecular ISM, $\mathcal{M}_{\text{mol}} \approx 5$ for the Zeeman, Mol dataset (Schneider et al. 2013). Assuming these Mach numbers and from the δv , δv_{turb} are computed for all three (pulsars, Zeeman, HI, and Zeeman, Mol) datasets using Eq. 6. The error in δv is propagated to compute the error in δv_{turb} , $\delta v_{\text{turb, err}}$.

Once δv_{turb} is known, $E_{\text{kin}} = 0.5 n \delta v_{\text{turb}}^2$ and $E_{\text{mag}} = B_{\text{los}}^2/8\pi$ is computed for all three datasets and the uncertainties in δv_{turb} and B_{los} are propagated to estimate uncertainties, $E_{\text{kin, err}}$ and $E_{\text{mag, err}}$ (n has a significantly low error compared to δv_{turb} , also for the pulsar samples because of the comparatively lower relative level of uncertainties in DM compared to both the H α and HI spectra, see Sec. 3.1 for further discussion). From now on in the paper, E_{mag} always refers to magnetic energy only along the line-of-sight and thus is the lower limit of the total magnetic energy.

3 RESULTS

In this section, we use the entire data, consisting of three datasets: pulsars probing the magnetic fields in the ionised ISM (ion), Zeeman, HI probing the magnetic fields in the atomic ISM (atm), and Zeeman, Mol probing the magnetic fields in the molecular ISM (mol) to show $E_{\text{mag}} \propto E_{\text{kin}}$ holds across all three phases (and equivalently over a large range of gas densities). We also discuss that the magnetic fields depend on both the gas density and turbulent velocity, not just the gas density as usually proposed by the $B - n$ relations.

3.1 $E_{\text{kin}} \propto E_{\text{mag}}$ instead of $B \propto n^{\text{factor}}$

First, in Fig. 1, we show the familiar B_{los} vs. n plot, especially including the pulsar data probing the ionised ISM in addition to Zeeman measurements. The pulsar data occupies significantly lower values of density ($3 \times 10^{-3} \text{ cm}^{-3} \lesssim n \lesssim 6 \times 10^{-1} \text{ cm}^{-3}$) for the diffuse ionised ISM, which also hosts statistically lower values of magnetic field strengths (see Fig. 3 (b) and Sec. 3.2 for further details). Based on the range of densities used to derive $B - n$ relations in the literature, we also show the broken power-law trend from Crutcher et al. (2010) for the atomic and molecular data and that from Whitworth et al. (2024) for the entire range of densities. The relationship in Whitworth et al. (2024) also seem to capture the ionised ISM well (note that they did not use the ionised ISM observations to derive the relation, they used a combination of dust polarisation and Zeeman observations).

Now, in Fig. 2, we show the relationship between E_{mag} and E_{kin} for the entire dataset, focussing on δv_{turb} for the ionised ISM derived using the H α and HI spectra in Fig. 2 (a) and Fig. 2 (b), respectively. For both cases, over the entire range of densities ($10^{-3} \text{ cm}^{-3} \lesssim n \lesssim 10^7 \text{ cm}^{-3}$), $E_{\text{mag}} \propto E_{\text{kin}}$. The data is fitted using a Monte Carlo-type method, where 5000 random samples are drawn in the xy -range ($E_{\text{kin}} \pm E_{\text{kin, err}}$, $E_{\text{mag}} \pm E_{\text{mag, err}}$) and fitted with a

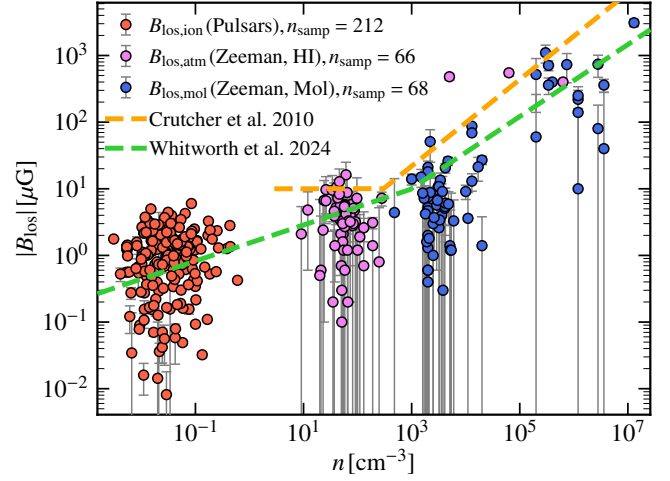


Figure 1. The relationship between density, n [cm^{-3}], and line-of-sight magnetic fields, B_{los} [μG], for Zeeman measurements probing atomic (Zeeman, HI) and molecular (Zeeman, Mol) ISM and for the ionised ISM added using pulsars in this work. n_{samp} represents the number of data points in each sample. The dashed orange and green lines show broken power-law relations taken from the literature. The Crutcher et al. 2010 line shows $10 \mu\text{G}$ for $n \lesssim n_{\text{crit}} \approx 300 \text{ cm}^{-3}$ and $10 \mu\text{G}(n/n_{\text{crit}})^{2/3}$ for $n > n_{\text{crit}}$ and the Whitworth et al. 2024 line shows $9.685 \mu\text{G}(n/n_{\text{crit}})^{0.27}$ for $n \lesssim n_{\text{crit}} \approx 924 \text{ cm}^{-3}$ and $9.685 \mu\text{G}(n/n_{\text{crit}})^{0.54}$ for $n > n_{\text{crit}}$. The Crutcher et al. 2010 relation is only shown across Zeeman, HI and Zeeman, Mol datasets as it was derived only for those range of densities whereas the Whitworth et al. 2024 relation was derived using a much larger range of densities (without studying the ionised phase though). The Whitworth et al. 2024 relation seems to better capture the data, also for the ionised ISM phase which was not used to derive that relation.

power-law, $E_{\text{mag}} = C_E E_{\text{kin}}^{\alpha_E}$ using LMFIT (Newville et al. 2015). Then the coefficient, C_E , and exponent, α_E , are estimated from the distributions to be the 50th percentiles and the corresponding errors are calculated as the difference between the 84th and 16th percentiles. For both the H α ($\delta v_{\text{turb, H}\alpha}$) and HI ($\delta v_{\text{turb, HI}}$) datasets, the coefficients and exponents (reported in the legends of Fig. 2) are similar, with the coefficient being slightly higher when $\delta v_{\text{turb, HI}}$ is used and exponent being slightly higher on using $\delta v_{\text{turb, H}\alpha}$. The uncertainties in E_{kin} with $\delta v_{\text{turb, H}\alpha}$ are higher than that for $\delta v_{\text{turb, HI}}$ (due to the smaller velocity channel width of the HI spectra, $\approx 1 \text{ km s}^{-1}$, compared to the H α spectra, 12 km s^{-1}) but the fitted parameters and associated errors are more driven by the significantly higher uncertainties in the E_{mag} values for both cases. Given the huge spread in E_{mag} , it is difficult to determine the exact fraction of the turbulent kinetic energy being converted to magnetic energy (this fraction might also strongly depend on the ISM phase) but $E_{\text{mag}} \propto E_{\text{kin}}$ holds true over all three phases (see Appendix B for the analysis with just the Zeeman measurements and Appendix C for the analysis which also includes plane-of-sky observations from dust polarisation measurements)¹. This also implies that the magnetic fields in the multiphase

¹ The uncertainties in the estimated density can significantly affect the derived $B - n$ relations (Tritsis et al. 2015; Jiang et al. 2020). To assess the impact of density uncertainties on the $E_{\text{mag}} - E_{\text{kin}}$ relation, we performed a numerical experiment in which we randomly assigned density uncertainties uniformly within a range of 10% to 300% of the respective density values for each point. We then reconstructed $E_{\text{kin, err}}$ and fit the $E_{\text{mag}} - E_{\text{kin}}$ relation, incorporating these density uncertainties. The differences in the fitted

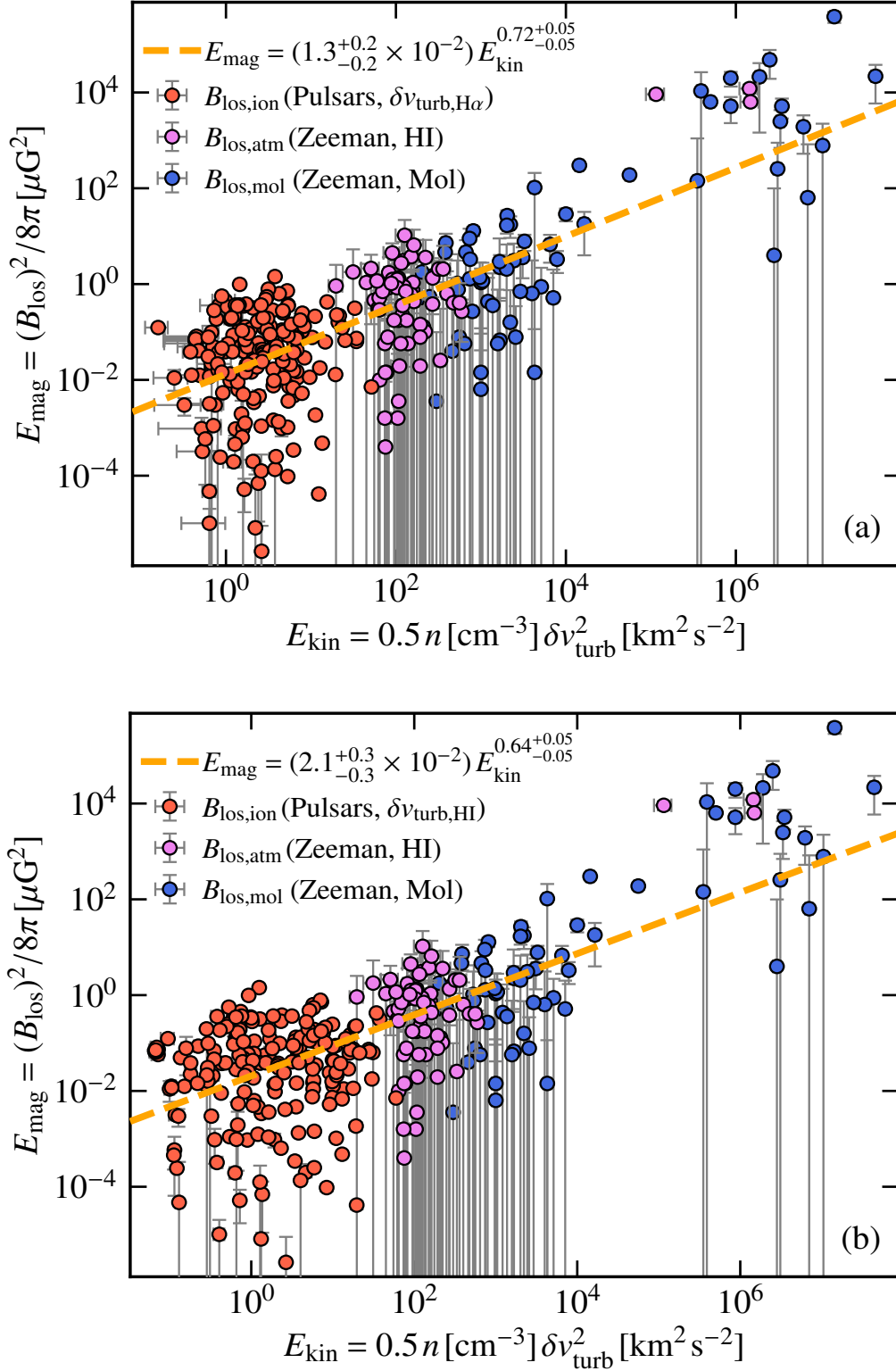


Figure 2. The turbulent kinetic, E_{kin} , and magnetic, E_{mag} , energy densities for the ionised (red, probed using pulsars), atomic (magenta, probed with Zeeman, HI), and molecular (blue, probed with Zeeman, Mol) ISM with a power-law fit (dashed orange line) for ionised gas turbulent velocities, δv_{turb} , computed using $\text{H}\alpha$ (panel (a), $\delta v_{\text{turb, H}\alpha}$) and HI (panel (b), $\delta v_{\text{turb, HI}}$) spectra. The uncertainties in E_{kin} values are higher for the $\text{H}\alpha$ case due to a larger velocity channel width of 12 km s^{-1} for the $\text{H}\alpha$ spectra as compared to $\approx 1 \text{ km s}^{-1}$ for the HI spectra. The exponent of the fitted power-law is slightly higher for the $\text{H}\alpha$ (a) case in comparison to the HI (b). But, for both cases, $E_{\text{mag}} \propto E_{\text{kin}}$, over all three phases and by extension a large range of E densities ($10^{-3} \text{ cm}^{-3} \lesssim n \lesssim 10^7 \text{ cm}^{-3}$, see Fig. 1).

Table 1. The mean (μ), standard deviation (σ), and relative level of fluctuations (σ/μ) of density (n), absolute value of the line-of-sight magnetic field ($|B_{\text{los}}|$), and turbulent velocity (δv_{turb}) for each ISM phase, ionised (ion), atomic (atm), and molecular (mol), obtained from the fit results shown in Fig. 3.

Quantity	Phase	μ	σ	σ/μ
n	ion	$\approx 0.025 \text{ cm}^{-3}$	$\approx 0.035 \text{ cm}^{-3}$	≈ 1.4
n	atm	$\approx 63 \text{ cm}^{-3}$	$\approx 30 \text{ cm}^{-3}$	≈ 0.5
n	mol	$\approx 3200 \text{ cm}^{-3}$	$\approx 2400 \text{ cm}^{-3}$	≈ 0.7
$ B_{\text{los}} $	ion	$\approx 1.3 \mu\text{G}$	$\approx 0.9 \mu\text{G}$	≈ 0.7
$ B_{\text{los}} $	atm	$\approx 4.0 \mu\text{G}$	$\approx 3.0 \mu\text{G}$	≈ 0.7
$ B_{\text{los}} $	mol	$\approx 6.3 \mu\text{G}$	$\approx 15.0 \mu\text{G}$	≈ 2.4
$\delta v_{\text{turb,H}\alpha}$	ion	$\approx 12.6 \text{ km s}^{-1}$	$\approx 0.0 \text{ km s}^{-1}$	≈ 0.0
$\delta v_{\text{turb,HI}}$	ion	$\approx 10.0 \text{ km s}^{-1}$	$\approx 4.8 \text{ km s}^{-1}$	≈ 0.5
δv_{turb}	atm	$\approx 2.0 \text{ km s}^{-1}$	$\approx 0.4 \text{ km s}^{-1}$	≈ 0.2
δv_{turb}	mol	$\approx 1.0 \text{ km s}^{-1}$	$\approx 0.7 \text{ km s}^{-1}$	≈ 0.7

ISM are determined by a combination of density and turbulent velocity (via E_{kin}) and do not only depend on the density as might be inferred from $B - n$ relations.

3.2 Probability distribution functions (PDFs) of density, magnetic fields, and turbulent velocities

Fig. 3 shows the probability density functions (PDFs) for n , $|B_{\text{los}}|$, $\delta v_{\text{turb,H}\alpha}$, and $\delta v_{\text{turb,HI}}$ for all three ionised (probed by pulsars, H α , and HI data), atomic (probed by Zeeman, HI), and molecular (probed by Zeeman, Mol) ISM. We fit a normal function, $\mathcal{N}(\mu, \sigma)$, to the PDF of \log_{10} of the variable for all the distributions assuming that the underlying variable follows a lognormal distribution. The fit is not equally good for all variables, especially n and $|B_{\text{los}}|$ in the molecular ISM show some sign of a bi-modal distribution. So, here, the normal function fit primarily captures the dominant peak. We discuss the choice of the lognormal functional form and, based on the fitted parameters (given in Table 1), the phase-wise properties and implications of each distribution below.

3.2.1 PDFs of n

A lognormal density distribution is usually associated with the turbulent origin of density structures in the ISM (Elmegreen & Scalo 2004). In the cold, molecular ISM, the gas density distribution is usually assumed to follow a lognormal (Vázquez-Semadeni 1994; Passot & Vázquez-Semadeni 1998; Federrath et al. 2008) or Hopkins (Hopkins 2013; Federrath & Banerjee 2015; Squire & Hopkins 2017; Beattie et al. 2022) PDF. The density PDF in star-forming regions might be even more complicated and, in addition to lognormal distribution, may include one or more power-law tails at higher densities (Burkhart 2018; Burkhart & Mocz 2019; Khullar et al. 2021; Appel et al. 2022, 2023; Mathew et al. 2024) or can be just a power-law (Alves et al. 2017). However, given the small sample size of the data in the Zeeman, Mol dataset ($n_{\text{samp}} = 68$), it is difficult to fit these complicated models and we only chose to fit a lognormal distribution. In the atomic and ionised regions, the multiphase

parameters, compared to those in Fig. 2, are negligible, as the uncertainties in the magnetic fields and turbulent velocities primarily dominate the overall uncertainties in the fit parameters.

ISM simulations show lognormal density distribution (de Avillez & Breitschwerdt 2005; Gent et al. 2013; Seta & Federrath 2022). The density distribution is also observationally shown to roughly follow a lognormal distribution in both the atomic (Burkhart et al. 2015) and ionised (Berkhuijsen & Fletcher 2008, 2015) ISM.

The density distribution for all three phases and their corresponding lognormal fits are shown in Fig. 3 (a). As expected, the mean of the distribution is significantly different between the phases, the mean of n is $\approx 0.025 \text{ cm}^{-3}$ in the ionised ISM, $\approx 63 \text{ cm}^{-3}$ in the atomic ISM, and $\approx 3200 \text{ cm}^{-3}$ in the molecular ISM. However, the relative density distribution is the widest in the diffuse (≈ 1.4) ionised ISM and has more comparable widths in the atomic (≈ 0.5) and molecular (≈ 0.7) phases (see Table 1).

3.2.2 PDFs of B_{los}

The structure of magnetic fields in the ISM is determined by a variety of physical processes: tangling of the large-scale (galactic, kpc scale) field, turbulent dynamo on scales comparable to the driving scale of ISM turbulence ($\approx 100 \text{ pc}$ for supernova explosions), and compression due to shocks (at a variety of scales). The turbulent dynamo and shock compression produce strongly intermittent, non-Gaussian magnetic fields (Zel'dovich et al. 1984; Ruzmaikin et al. 1989; Schekochihin et al. 2004; Seta et al. 2020; Seta & Federrath 2021a, 2022; Sur & Subramanian 2024), whereas the tangling of the large-scale field will likely produce Gaussian fields due to the volume filling nature of the ISM turbulence (see Appendix A in Seta et al. 2018 and Sec. 4.1 in Seta & Federrath 2020). Thus, the resulting magnetic field would be a mixture of both Gaussian and non-Gaussian components. Given that the contribution from each component is not known and the small sample size ($n_{\text{samp}} = 212, 66,$ and 68 in ion, atm, and mol phases), we assume B_{los} follows a normal distribution and thus fit a lognormal function to the PDF of $\log_{10}(|B_{\text{los}}|/1 \mu\text{G})$.

Fig. 3 (b) shows the PDF of $\log_{10}(|B_{\text{los}}|/1 \mu\text{G})$ for all three ion, atm, and mol phases. The mean value of magnetic fields is stronger in the denser regions, increasing from the ionised ($\approx 1.3 \mu\text{G}$) to atomic ($\approx 4.0 \mu\text{G}$) to molecular ($\approx 6.3 \mu\text{G}$) phases but there is a significant overlap between the three PDFs. Moreover, the width in the ionised ISM ($\approx 0.9 \mu\text{G}$) is lower than that in the cold atomic phase ($\approx 3 \mu\text{G}$) but the width is significantly higher in the molecular phase ($\approx 15 \mu\text{G}$). This further demonstrates that the magnetic fields respond to the ISM properties other than the gas density (compare relative widths in Fig. 3 (a) and Fig. 3 (b), also see Table 1) and the $B \propto n^{\text{factor}}$ does not hold across all the ISM phases as $E_{\text{mag}} \propto E_{\text{kin}}$ does (Fig. 2). Moreover, the relative fluctuations (standard deviation/mean) in the ionised and atomic phases are similar (≈ 0.7), it is significantly higher in the molecular phase (≈ 2.4).

3.2.3 PDFs of $\delta v_{\text{turb,H}\alpha}$ and $\delta v_{\text{turb,HI}}$

Turbulence in the ISM is driven by a variety of processes at a range of scales (Elmegreen & Scalo 2004; Scalo & Elmegreen 2004; Mac Low & Klessen 2004) and the ISM turbulence is also expected to be a combination of spatially intermittent, non-Gaussian and Gaussian components (see Sec. 3.2 in Hennebelle & Falgarone 2012, for a discussion). However, like magnetic fields, due to the lack of proper characterisation of the ISM turbulent velocities and given the limited data size, we assume that the underlying turbulent velocities follow a normal distribution and fit a lognormal function to the PDF of $\log_{10}(\delta v_{\text{turb}}/1 \text{ km s}^{-1})$.

Fig. 3 (c) and Fig. 3 (d) shows the PDFs of $\log_{10}(\delta v_{\text{turb}}/1 \text{ km s}^{-1})$

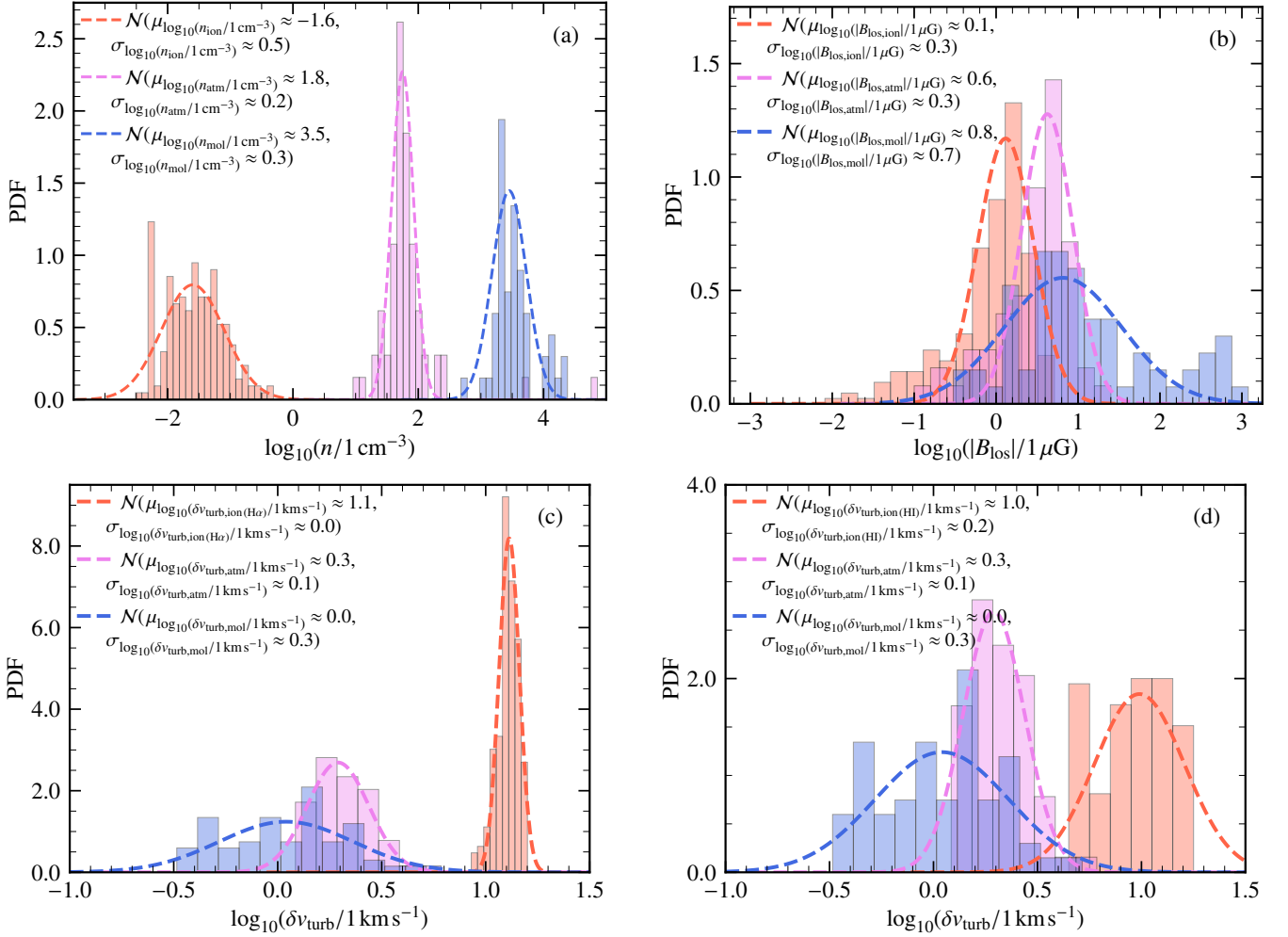


Figure 3. Probability density functions (PDFs) for gas density, n (panel (a)), the absolute value of line-of-sight magnetic fields, $|B_{\text{los}}|$ (panel (b)), and turbulent velocities, $\delta v_{\text{turb,H}\alpha}$ (panel (c)) and $\delta v_{\text{turb,HI}}$ (panel (d)), for ionised (ion), atomic (atm), and molecular (mol) phases of the ISM. For all the distributions, we fit a lognormal function to the PDF (the current data size and quality is insufficient to fit further complicated models, see the text in Sec. 3.2 for further discussion), and the estimated mean and standard deviation of the underlying normal distribution are reported in the legend. The sharp peak for $\delta v_{\text{turb,H}\alpha}$ at $\log_{10}(\delta v_{\text{turb,ion(H}\alpha)}/1 \text{ km s}^{-1}) \approx 1.1$, which implies $\langle \delta v_{\text{turb,H}\alpha} \rangle \approx 12.6 \text{ km s}^{-1}$, might be due to the large channel width of the H α spectra ($= 12 \text{ km s}^{-1}$). In comparison, $\delta v_{\text{turb,HI}}$ (spectral channel width $\approx 1 \text{ km s}^{-1}$) distribution shows a much wider distribution and might better probe the turbulence along the pulsar sightlines. Even though the densities between the three phases are well-separated, there is a significant overlap in the corresponding magnetic field distributions. The width of the magnetic field distribution is highest for the molecular ISM and that is a combination of (relatively wider) turbulent velocity and density distributions (note that the density distribution is the widest for the ionised ISM). This further emphasises that the properties of the ISM magnetic fields are determined by both the density and turbulent velocity and not just the density. The corresponding quantification in terms of the mean and standard deviation of the fitted distributions is given in Table 1.

and their corresponding fits for all three phases. It is inherently difficult to directly compare $\delta v_{\text{turb,H}\alpha}$ and $\delta v_{\text{turb,HI}}$ distributions due to an order of magnitude difference in their spectral velocity channel widths ($\approx 1 \text{ km s}^{-1}$ for HI and 12 km s^{-1} for H α). For the $\delta v_{\text{turb,H}\alpha}$ case (Fig. 3 (c)), there is practically no overlap between the turbulent velocities in the ionised phase and the other two phases, which show some overlap. However, we caution that the mean of $\delta v_{\text{turb,H}\alpha}$ distribution $\approx 12.6 \text{ km s}^{-1}$ (very close to the channel width) and very small width might be due to the large-channel width of the H α spectra. For the $\delta v_{\text{turb,HI}}$ case (Fig. 3 (d)), the mean value of turbulent velocity distribution decreases from the ionised ($\approx 10 \text{ km s}^{-1}$) to atomic ($\approx 2 \text{ km s}^{-1}$) to molecular ($\approx 1 \text{ km s}^{-1}$) ISM but the relative width is highest for the molecular phase (0.7, see Table 1). So, even though the density shows a lower relative width in for the molecular ISM (Fig. 3 (a)), the large width in the magnetic field distribution

(Fig. 3 (b)) might be due to a wider turbulent velocity distribution. Moreover, for the ionised ISM, the wider density distribution does not necessarily result in a wider magnetic field distribution probably because of comparatively less wide turbulent velocity distribution (compare numbers across phases in Table 1). These inferences further emphasise that the ISM magnetic fields are determined by both the density and turbulent velocities and not just the density.

3.3 Phase-wise importance of magnetic fields

The importance of magnetic fields is usually characterised by plasma beta, which is the ratio of the thermal to magnetic pressure. We define it as

$$\beta_{\text{plasma}} = nk_{\text{B}}T / (B_{\text{los}}^2 / 8\pi), \quad (7)$$

Table 2. The density (n), temperature (T), absolute value of the line-of-sight magnetic field ($|B_{\text{los}}|$), and plasma beta (β_{plasma} , Eq. 7, the upper limit of the conventional plasma beta since only the line-of-sight field strength used) for all three phases. n and $|B_{\text{los}}|$ are taken from Table 1 and T is assumed for each phase to compute β_{plasma} . In all the phases, the magnetic pressure is comparable to the thermal pressure, further demonstrating that magnetic fields are an important component of all the ISM phases.

Phase	n [cm^{-3}]	T [K]	$ B_{\text{los}} $ [μG]	β_{plasma}
Ionised	$\approx 0.025 \text{ cm}^{-3}$	$\approx 10^4 \text{ K}$	$\approx 1.3 \mu\text{G}$	≈ 0.5
Atomic	$\approx 63 \text{ cm}^{-3}$	$\approx 10^2 \text{ K}$	$\approx 4.0 \mu\text{G}$	≈ 1.4
Molecular	$\approx 3200 \text{ cm}^{-3}$	$\approx 10 \text{ K}$	$\approx 6.3 \mu\text{G}$	≈ 3.0

where n is the number density, k_B is the Boltzmann constant, T is the temperature, and B_{los} is the line-of-sight magnetic field. In principle, the definition involves the total magnetic field strength but we use the available B_{los} values, so, β_{plasma} computed this way is actually the upper limit of the plasma beta. The higher values of β_{plasma} ($\gg 1$) imply that magnetic fields have negligible impact and could be ignored, $\beta_{\text{plasma}} \approx 1$ correspond to magnetic pressure being as important as the thermal pressure, and $\beta_{\text{plasma}} \ll 1$ corresponds to the situation where magnetic pressure is dynamically more important than the thermal pressure. From this work, we have phase-wise information of n and B_{los} , and we source T in each phase from the literature. We assume $T \approx 10^4 \text{ K}$ for the ionised phase (warm ionised gas probed by the pulsars), $T \approx 10^2 \text{ K}$ for the atomic phase (the dense gas, see Table 1, probed by the Zeeman effect is majorly the cold atomic medium), and $T \approx 10 \text{ K}$ for the molecular phase (Ferrière 2001, 2020). The estimated β_{plasma} values are given in Table 2. We emphasise that these values represent typical numbers in each phase and, in principle, the plasma beta would also have a distribution. For all the phases, we find $\beta_{\text{plasma}} \approx 1$, and thus the magnetic pressure is comparable to the thermal pressure. This further demonstrates that the magnetic fields are an important component of all the ISM phases and their dynamical impact should not be ignored.

4 DISCUSSION

4.1 Further confirmation of the analysis for the ionised ISM

For the results and discussion in Sec. 3, we treated all three observational datasets, pulsars, Zeeman, HI, and Zeeman, Mol equally. However, there are two primary differences between the analysis with the pulsar data and Zeeman measurements. First, the turbulent velocities for the Zeeman measurements are derived using the Zeeman data itself, whereas, for pulsars, the turbulent velocities are estimated from independent H α and HI observations. Second, and more importantly, the gas density and line-of-sight magnetic fields in the Zeeman data probe localised regions of the ISM, whereas the pulsars give the *average* gas density (Eq. 3) and line-of-sight magnetic fields (Eq. 4) over the entire path-length. We assume these average values as representative numbers in the ionised ISM. Here, using the observational dataset (Sec. 4.1.1) and multiple multiphase ISM simulations (Sec. 4.1.2), we demonstrate that these are fair assumptions and further confirm our analysis using the pulsar and HI data for the ionised ISM.

4.1.1 Length scales in the ionised ISM

To test the effect of averaging over large length scales ($= L_{\text{pul}}$, distance to the pulsar) in the analysis for the ionised ISM, we divide the pulsar sample into two groups. Once by the Galactic latitude, $|\text{Gal. Lat.}| = 5^\circ$ (Fig. 4 (a)), and next by the distance to the pulsar, $L_{\text{pul}} = 2 \text{ kpc}$ (Fig. 4 (b)). For both cases, the motivation is to test whether the $E_{\text{mag}} \propto E_{\text{kin}}$ relation shows any variation with more of the ISM along the line-of-sight – either by probing more of the Galactic plane or due to a longer line of sight. The cutoff Galactic latitude, $|\text{Gal. Lat.}| = 5^\circ$, and distance, $L_{\text{pul}} = 2 \text{ kpc}$, are reasonably chosen based on the fact that they yield roughly similar numbers of pulsars in each latitude/distance bin.

In Fig. 4 (a), we separate the pulsars using the Galactic latitude (Gal. Lat.) to probe the ISM close to the Galactic plane ($|\text{Gal. Lat.}| \leq 5^\circ$) and the pulsars located away from the plane ($|\text{Gal. Lat.}| > 5^\circ$). The pulsars close to the plane probe the ionised ISM with statistically larger values of E_{kin} (due to higher n and δv_{turb}), while that for away samples are averaged over regions with significantly lower values of n and δv_{turb} . This gives rise to some separation along the $E_{\text{mag}} \propto E_{\text{kin}}$ fit (dashed orange line in Fig. 4 (a)) but there is no preference for either group to be close to the fitted line. Both groups show an equal level of spread across it.

Next, in Fig. 4 (b), we divide the pulsar sample into two groups based on the distance to the pulsar, $L_{\text{pul}} \leq 2 \text{ kpc}$ and $L_{\text{pul}} > 2 \text{ kpc}$. Both groups show equal spread along and across the $E_{\text{mag}} \propto E_{\text{kin}}$ fit (dashed orange line in Fig. 4 (b)). These tests (Fig. 4) demonstrate that averages of thermal electron density and line-of-sight magnetic fields over the kpc distances to the pulsars are good representatives of typical density and line-of-sight magnetic field strength in the ionised ISM.

4.1.2 Confirmation from multiphase ISM simulations

To further check the $E_{\text{mag}} \propto E_{\text{kin}}$ relation in the ionised ISM phase, we use two types of multiphase ISM simulations: numerically driven turbulence, two-phase simulations from Seta & Federrath (2022) and supernova driven, three-phase TIGRESS (Three-phase Interstellar Medium in Galaxies Resolving Evolution with Star Formation and Supernova Feedback) simulations from Kado-Fong et al. (2020). We first give here basic overall details of each type of simulation and then describe the construction of E_{mag} and E_{kin} using it.

The first type of simulation is taken from Seta & Federrath (2022), where turbulence is driven numerically at a scale of 100 pc in a three-dimensional, triply-periodic domain (512^3 grid points) of size 200 pc along each dimension with Milky Way-type heating and cooling functions. The turbulence is driven both solenoidally, Sol, and compressively, Comp (see Federrath et al. 2008, for further details). The equations for non-ideal magnetohydrodynamics are solved and the corresponding viscosity and resistivity are chosen to be a factor of ≈ 4 times higher than their expected numerical values. Further details of the setup and initial conditions are described in Sec. 2 of Seta & Federrath (2022). The initial weak magnetic fields (random field of strength $10^{-4} \mu\text{G}$) amplify due to the turbulent dynamo mechanism, achieving a statistically steady state. We take hydrogen number density (n_{H}), temperature (T), velocity, and magnetic fields from a snapshot in this statistically steady state. The thermal electron density, n_e , needed to compute mock DM and RM from these simulations is computed using n_{H} and T as (Hollins et al. 2017)

$$n_e = n_{\text{H}} \left[\frac{\arctan(T/10^3 \text{ K} - 10)}{\pi} + \frac{1}{2} \right]. \quad (8)$$

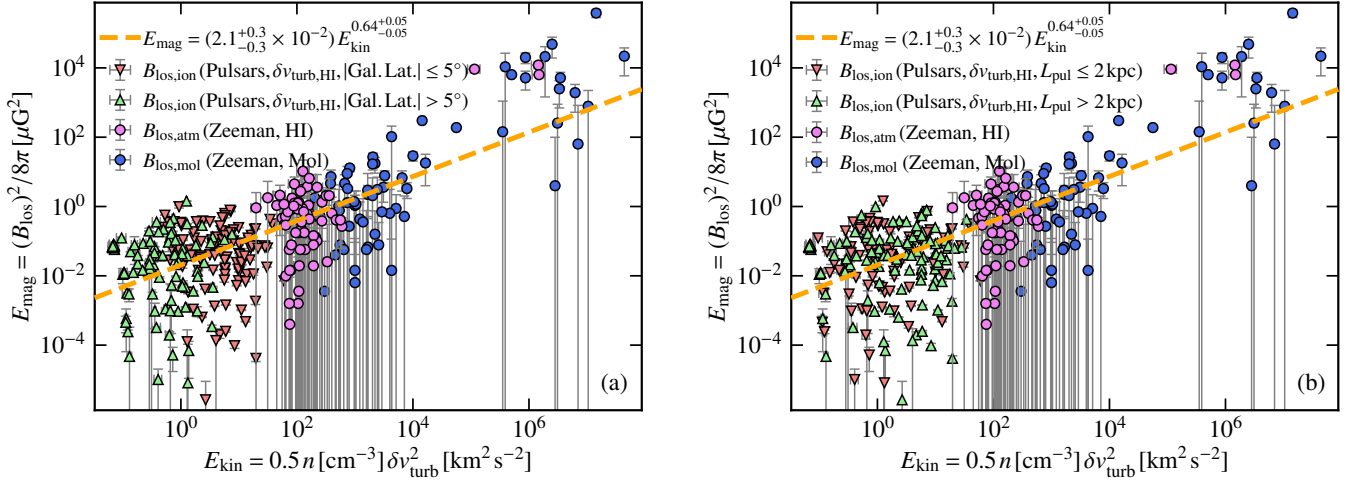


Figure 4. To test the influence of averaging over large, of the order of kpcs, length scales to derive the $E_{\text{mag}} - E_{\text{kin}}$ relation in the ionised ISM from the pulsar observations (Sec. 2.2), we divide the data into groups by the Galactic latitude (Gal. Lat.) of the pulsar (panel (a)) and the distance to the pulsar (panel (b), L_{pul}). When divided by the Gal. Lat. (a), Gal. Lat. $\leq 5^\circ$ ($n_{\text{samp}} = 108$) and Gal. Lat. $> 5^\circ$ ($n_{\text{samp}} = 104$), the pulsars in the lower Galactic latitude tend to probe larger values of E_{kin} due to higher densities and turbulent velocities in the Galactic plane. But neither group shows a preference to be closer to $E_{\text{mag}} \propto E_{\text{kin}}$ fit (dashed orange line). On the other hand, when divided by L_{pul} , $L_{\text{pul}} \leq 2 \text{ kpc}$ ($n_{\text{samp}} = 85$) and $L_{\text{pul}} > 2 \text{ kpc}$ ($n_{\text{samp}} = 127$), the pulsars are randomly distributed along and across the $E_{\text{mag}} \propto E_{\text{kin}}$ fit. These tests confirm that the average values of density and line-of-sight magnetic fields used to compute E_{mag} and E_{kin} from the pulsar sample are representative of the ionised ISM in spite of the averaging.

For the second type, we take TIGRESS simulations (data sourced from <https://princetonuniversity.github.io/astro-tigress>), which represents the solar neighbourhood conditions and includes galactic shear, self-gravity, star particles, turbulence driven by self-consistent supernova feedback, and relevant cooling and heating functions (Kim & Ostriker 2017). They start their simulations with a relatively strong magnetic field (uniform field of strength $2.6 \mu\text{G}$) and solve ideal magnetohydrodynamics equations for 660 Myr. The chosen model (R8_2pc_0300) has a size of $1024 \text{ pc} \times 1024 \text{ pc} \times 7168 \text{ pc}$ (xy represent the Galactic plane and z the vertical direction) with a uniform grid spacing of 2 pc and is at a time of 300 Myr in the evolution. Then, using n_{H} , T , and properties of star particles, the authors post-process the data using ray-tracing and ionisation calculation (see Sec. 2 in Kado-Fong et al. 2020, for further details) to determine the equilibrium fraction of the atomic component, which can be further used to compute n_{e} . From the TIGRESS dataset, we take n_{H} , T , velocity, magnetic fields, and n_{e} .

We use the data from these simulations and repeat the entire analysis done for the ionised ISM using pulsar observations (Sec. 2.2 and Sec. 2.3). First, knowing n_{e} , choosing a line-of-sight (along \hat{y} for both types of simulations), and utilising the entire domain as path length (200 pc for Sol and Comp datasets and 1024 pc for the TIGRESS data), we compute mock DM and RM using Eq. 1 and Eq. 2, respectively. Then, from the mock DM and RM, using Eq. 3 and Eq. 4, we compute $\langle n_{\text{e}} \rangle$ and $\langle B_{\text{los}} \rangle$. As with the pulsar data, we assume that these represent typical gas density and line-of-sight magnetic field for the ionised ISM, i.e., $n \approx \langle n_{\text{e}} \rangle$ and $B_{\text{los}} \approx \langle B_{\text{los}} \rangle$. Next, using density, temperature and line-of-sight velocity (velocity along \hat{y} direction), we perform the radiative transfer calculation to generate mock HI emission spectra using the formalism in Sec 2.2 of Bhattacharjee et al. (2024) (also, see Miville-Deschênes et al. 2003). Then, using Eq. 5, we compute δv for each line-of-sight and, like for pulsars, assume the Mach number in the ionised ISM $\mathcal{M}_{\text{ion}} \approx 1$ to compute $\delta v_{\text{turb,HI}}$. Finally, using B_{los} , n , and $\delta v_{\text{turb,HI}}$, E_{mag} and E_{kin} are constructed.

From the obtained E_{mag} and E_{kin} , 10000 random points are se-

lected and are fit with a power-law, $E_{\text{mag}} = C_E E_{\text{kin}}^{\alpha_E}$, for all three simulated datasets, Sol, Comp, and TIGRESS. The data and the determined fit for each simulated dataset are shown in Fig. 5. The Sol case does not show any significant relation between E_{mag} and E_{kin} , but this might also be because of a small range of E_{kin} (x -axis in Fig. 5 (a)). The large scatter seen in the simulated data compared to the observations in Fig. 2 may be more evident here due to the limited range on the x -axis or is expected at lower densities because of the physics of different magnetohydrodynamic modes (Passot & Vázquez-Semadeni 2003; Vázquez-Semadeni et al. 2024). For cases with a significant E_{kin} range (at least an order of magnitude), Comp in Fig. 5 (b) and TIGRESS in Fig. 5 (c), $E_{\text{mag}} \propto E_{\text{kin}}$. Both the coefficient, C_E , and exponent, α_E , are significantly different between the two and those in the observational results shown in Fig. 2. This might be due to differences in the physics modelled in these simulations and further complexities in observations (line-of-sight effects, the influence of the Local Bubble, bias in pulsar locations, multiscale magnetic field and thermal electron density structures, observational effects, etc.). Understanding these differences requires further work and more pulsars with independent distances. However, the general trend of proportionality between the E_{mag} and E_{kin} confirms our method for the ionised ISM, especially the idea of combining n obtained from the pulsar DM observations with δv_{turb} from HI spectra to compute E_{kin} .

4.2 ISM magnetic fields are determined by both the density and turbulent velocity

In Sec. 3, using both the $E_{\text{mag}} - E_{\text{kin}}$ relation (Fig. 2) and relative differences between the PDFs of density, magnetic fields, and turbulent velocities with the ISM phase (Fig. 3 and Table 1), we demonstrated that the magnetic field depends on both the density and turbulent velocity and not just the density as, at times, inferred from the magnetic field - density relations. However, we showed this only for the magnetic field strengths. The magnetic field structure might also depend on both the density and turbulent velocity structures. In the

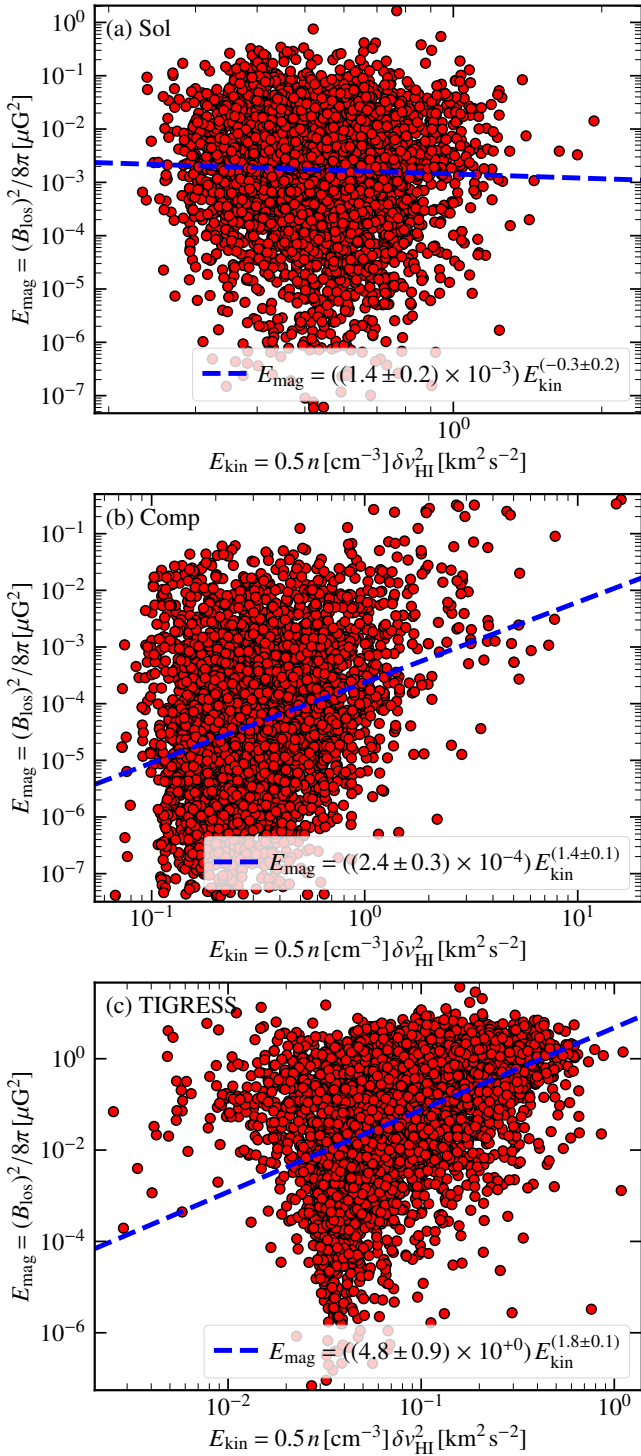


Figure 5. The $E_{\text{mag}} - E_{\text{kin}}$ relation derived from observations (Fig. 2) is tested only for the ionised ISM using two-types of multiphase ISM simulations: two-phase, numerically driven turbulence simulations (Sol, panel (a) and Comp, panel (b)) and three-phase, supernova driven turbulence simulations (TIGRESS, panel (c)). For these simulations, we use the analysis exactly as done for the ionised ISM (Sec. 2.2 and Sec. 2.3). From the mock observations, for each case, 10000 points (red) are randomly selected and fitted with a power-law (dashed blue line). For the Sol case, E_{mag} does not show a significant dependence on E_{kin} and this is due to a very small range of values in E_{kin} (x-range). On the other hand, both Comp and TIGRESS cases show a power-law dependence. The exact coefficient and exponent in the power-law fit depends on the physics included in the simulations but $E_{\text{mag}} \propto E_{\text{kin}}$ holds true for both those cases.

literature, both aspects are individually discussed. The atomic hydrogen filaments are shown to be aligned with the ISM magnetic fields, suggesting a more density-magnetic field connection in terms of the structure (Clark et al. 2014, 2019; Ma et al. 2023). There are also discussions associating these structures more with the turbulent velocity properties (Lazarian & Pogosyan 2000; Yuen et al. 2019, 2021). In principle, both could be right and the contribution from each would depend on the phase, length scales, and the type of observable. For example, the synchrotron polarisation probes more of the warm, ionised ISM, where turbulent velocities might play a dominant role and the dust polarisation probes more of the colder ISM, where the density fluctuations might play a major role. Separating the contribution from the density and turbulent velocity structures to magnetic structures requires further work, which we aim to do in the future.

4.3 Assumptions and missing effects

Throughout the analysis, we have made some simplifying assumptions and, here, we discuss them and their possible implications on the derived results.

To compute the velocity widths from the all-sky H α and HI spectra, we associated features within velocities of $\pm 50 \text{ km s}^{-1}$ with the Milky Way. This choice is motivated by the fact we would like to avoid the isolated high-velocity clouds (usually at absolute velocities greater than 90 km s^{-1} , see Wakker & van Woerden 1997) as they may not represent the typical ISM along pulsar sight lines, which samples a very heterogeneous region of the Milky Way’s ISM. Moreover, from a larger HI absorption sample (BIGHiCAT from McClure-Griffiths et al. 2023), most Milky Way features are observed within absolute velocities of $\approx \pm 60 \text{ km s}^{-1}$ (Rybarczyk et al. 2024). We vary our limits of cutoff velocities from $\pm 50 \text{ km s}^{-1}$ to $\pm 60 \text{ km s}^{-1}$. This made negligible difference to results in Fig. 2 and Fig. 3 (c, d) and thus do not alter any of our conclusions.

For the ionised ISM, when computing δv_{turb} for E_{kin} from the HI emission spectra (Sec. 2.3 and Sec. 2.4), we assumed the $\mathcal{M}_{\text{atm}} \approx 1$. In principle, the HI emission spectra have contributions from both the warm and cold atomic, neutral medium (Wolfire et al. 1995, 2003) and the cold atomic medium has significantly higher Mach number ($\gtrsim 3$, Heiles & Troland 2003b; Murray et al. 2015; McClure-Griffiths et al. 2023). However, on an average, the HI emission spectra are dominated by the volume-filling, warm atomic component, so the contribution from the localised cold atomic medium (which is primarily probed by the HI absorption spectra) is sub-dominant. Moreover, even though pulsar observations probe the ionised ISM, we associate the turbulent velocities computed from the HI spectra (in emission) with those. This assumes that, on average, the turbulent velocities in the atomic ISM are comparable to the turbulent velocities in the ionised ISM (see Table 2 in Ferrière 2020). Note that we also use the H α spectra, which indeed probes the ionised ISM and the $E_{\text{mag}} - E_{\text{kin}}$ relation are very similar for both the H α and HI cases (Fig. 2). Moreover, in principle, \mathcal{M} in each phase might also have some variation with the line-of-sight but the currently available data is insufficient to include such a variation in the analysis.

We have only considered the line-of-sight components of magnetic fields and turbulent velocities to compute E_{mag} and E_{kin} . In principle, the component perpendicular to the line of sight can be different for both and need not necessarily be correlated. This assumption also, in some sense, is connected to the isotropy of 3D small-scale structures in the ISM. These 3D structures might be anisotropic (e.g. filaments and sheets), and that might introduce corrections to the derived $E_{\text{mag}} \propto E_{\text{kin}}$ relation. For the ionised ISM, the large distances

to pulsars lead to density and magnetic fields being averaged over multiple such smaller-scale structures and this has been further tested in Sec. 4.1. Moreover, for the ionised ISM, the angular beam size is significantly smaller for the pulsar data (pencil beam) in comparison to the $H\alpha$ (1 deg) and HI (10.8 arcmin or 16.2 arcmin, depending on the survey, see Sec. 2.3) data. But we do not expect this to make a significant difference to the derived results as, again assuming isotropy of 3D small-scale structures in the ISM, averaging along the line-of-sight (for pulsar RMs and DMs) will have a similar effect as averaging on the plane-of-sky (for $H\alpha$ and HI spectra).

We have assumed a single power-law function to capture the relationship between E_{mag} and E_{kin} across all the ISM phases. From the multiphase simulations of the turbulent dynamo in the ISM, it is expected that the ratio of $E_{\text{mag}}/E_{\text{kin}}$ depends on the phase of the ISM ($E_{\text{mag}}/E_{\text{kin}} \approx 0.1$ in the warm phase and ≈ 0.01 in the cold phase, see Seta & Federrath 2022). So, with the changing ISM phase, from ionised to atomic to molecular, the amplitude of the power-law function might change. This is difficult to explore with the current number of data points in each phase ($n_{\text{samp}} = 212$ in the ionised ISM, $n_{\text{samp}} = 66$ in the atomic ISM, and $n_{\text{samp}} = 68$ in the molecular ISM) and given the large uncertainty in the magnetic field estimates. With much larger and more precise data, a more complicated fit function, possibly three power-laws with the same exponent but different coefficients, can be attempted.

Overall, with the available data, the analysis here allowed us to explore the relationship between E_{mag} and E_{kin} over the three ISM phases (ionised, atomic, and molecular). In our future work, we aim to explore some of these additional effects using new observations and simulations.

5 SUMMARY AND CONCLUSION

Magnetic fields are an important component of the interstellar medium (ISM) of galaxies, but their connection with the multiphase ISM gas is yet to be completely known. Usually, to account for magnetic fields' impact on star formation, a relationship between the magnetic field strength, B , and gas density, n , is assumed. Here, for the Milky Way, in addition to Zeeman measurements of line-of-sight magnetic fields, B_{los} , in the atomic and molecular ISM, we supplement B_{los} measurements in the ionised ISM using pulsar observations. This allows us to explore the magnetic fields across all three ISM phases, ionised, atomic, and molecular and by extension a large range of gas densities ($10^{-3} \text{ cm}^{-3} \lesssim n \lesssim 10^7 \text{ cm}^{-3}$). In particular, we study the relationship between the turbulent kinetic energy, E_{kin} , and magnetic energy, E_{mag} .

The Zeeman observations (described in Sec. 2.1) provide n , B_{los} , and velocity widths of the components, δv , but the pulsars observations only provide the average thermal electron density, $\langle n_e \rangle$ (Eq. 3), and average line-of-sight magnetic field, $\langle B_{\text{los}} \rangle$ (Eq. 4), where averages are over the distance to the pulsar. So, for the ionised ISM, we perform two further steps in our analysis (Sec. 2.2). First, for each pulsar line-of-sight, we use both the ionised ($H\alpha$) and atomic (HI) hydrogen spectra to compute δv along that line of sight (Sec. 2.3). Second, we assume that, for the ionised ISM, gas with density $n \approx \langle n_e \rangle$ hosts line-of-sight magnetic fields $B_{\text{los}} \approx \langle B_{\text{los}} \rangle$ (tested and discussed using observations and multiphase simulations in Sec. 4.1). Then, for all the three ISM phases, we assume a Mach number, \mathcal{M} , to compute the turbulent velocity, δv_{turb} , from the observed (atomic and molecular) and computed (ionised) δv , where we assume $\mathcal{M}_{\text{ion}} \approx \mathcal{M}_{\text{atm}} \approx 1$ and $\mathcal{M}_{\text{mol}} \approx 5$ (Sec. 2.4). Finally, with the data (n , B_{los} , δv_{turb}) we

compute the $E_{\text{mag}} = B_{\text{los}}^2/8\pi$ and $E_{\text{kin}} = 0.5 n \delta v_{\text{turb}}^2$ for all three ionised, atomic, and molecular phases.

We find that $E_{\text{mag}} \propto E_{\text{kin}}$ across all the ISM phases (Fig. 2 and Sec. 3.1), and it is a more concrete relationship in comparison to $B \propto n^{\text{factor}}$ as a power-law works across all the phases and over a large range of densities. It is also more physically motivated by the idea that a fraction of turbulent kinetic energy is converted to magnetic energy and does not require details of the geometry of the gas packet and local magnetic field orientation as usually necessary before applying the $B - n$ relations. Furthermore, using the probability distribution function of density, magnetic fields, and turbulent velocities (Fig. 3, Table 1, and Sec. 3.2), we show that the magnetic field fluctuations are decided by both the density and turbulent velocity fluctuations. Finally, we also compute the typical plasma beta (Table 2 and Sec. 3.3) and show that the magnetic pressure is comparable to the thermal pressure in all the ISM phases. In conclusion, our work demonstrates that magnetic fields are a dynamically important component of the ionised, atomic, and molecular ISM, determined by both gas density and turbulent velocity.

ACKNOWLEDGEMENTS

We thank the anonymous referee for their fast and productive report. A. S. thanks Christoph Federrath, Bryan M. Gaensler, Yik Ki Ma, Antoine Marchal, Aris Tritsis, Richard M. Crutcher, Enrique Vázquez-Semadeni, Timothy Robishaw, Alex S. Hill, and Chong-Chong He for useful discussions. We thank Kate Pattle for providing the data used in Appendix C. The authors acknowledge Interstellar Institute's program "II6" and the Paris-Saclay University's Institut Pascal for hosting discussions that nourished the development of the ideas behind this work. A. S. acknowledges support from the Australian Research Council's Discovery Early Career Researcher Award (DECRA, project DE250100003). We also acknowledge funding provided by the Australian Research Council (Discovery Project DP220101558 and Laureate Fellowship FL210100039 awarded to N. M. Mc-G.).

DATA AVAILABILITY

This work uses available data from the literature: Zeeman measurements from Crutcher et al. (2010), pulsars data from <https://www.atnf.csiro.au/research/pulsar/psrcat> (version 2.4.0, Manchester et al. 2005), $H\alpha$ data from <https://www.astro.wisc.edu/research/research-areas/galactic-astronomy/wham/wham-sky-survey> (Haffner et al. 2003, 2010), HI data from https://www.astro.uni-bonn.de/hisurvey/AllSky_gauss (McClure-Griffiths et al. 2009; Kalberla et al. 2010; Winkel et al. 2016), and Davis-Chandrasekhar-Fermi (DCF) measurements (used in Appendix C) from Pattle et al. (2023). The multiphase ISM simulation data used in Sec. 4.1.2 is taken from Seta & Federrath (2022) and Kado-Fong et al. (2020). The analysed data underlying this article will be shared on a reasonable request to the corresponding author, Amit Seta (amit.seta@anu.edu.au).

REFERENCES

- Achikanath Chirakkara R., Federrath C., Trivedi P., Banerjee R., 2021, *Phys. Rev. Lett.*, **126**, 091103
Alves J., Lombardi M., Lada C. J., 2017, *Astron. Astrophys.*, **606**, L2

- Appel S. M., Burkhart B., Semenov V. A., Federrath C., Rosen A. L., 2022, *Astrophys. J.*, 927, 75
- Appel S. M., Burkhart B., Semenov V. A., Federrath C., Rosen A. L., Tan J. C., 2023, *Astrophys. J.*, 954, 93
- Beattie J. R., Mocz P., Federrath C., Klessen R. S., 2022, *Mon. Not. R. Astron. Soc.*, 517, 5003
- Beck R., 2016, *Ann. Rev. Astron. Astrophys.*, 24, 4
- Beck R., Brandenburg A., Moss D., Shukurov A., Sokoloff D., 1996, *Ann. Rev. Astron. Astrophys.*, 34, 155
- Beck R., Shukurov A., Sokoloff D., Wielebinski R., 2003, *Astron. Astrophys.*, 411, 99
- Berkhuijsen E. M., Fletcher A., 2008, *Mon. Not. R. Astron. Soc.*, 390, L19
- Berkhuijsen E. M., Fletcher A., 2015, *Mon. Not. R. Astron. Soc.*, 448, 2469
- Berkhuijsen E. M., Mitra D., Mueller P., 2006, *Astronomische Nachrichten*, 327, 82
- Bernet M. L., Miniati F., Lilly S. J., Kronberg P. P., Dessauges-Zavadsky M., 2008, *Nature*, 454, 302
- Bhattacharjee S., Roy N., Sharma P., Seta A., Federrath C., 2024, *Mon. Not. R. Astron. Soc.*, 527, 8475
- Brandenburg A., Ntormousi E., 2023, *Ann. Rev. Astron. Astrophys.*, 61, 561
- Brandenburg A., Subramanian K., 2005, *Phys. Rep.*, 417, 1
- Burkhart B., 2018, *Astrophys. J.*, 863, 118
- Burkhart B., Mocz P., 2019, *Astrophys. J.*, 879, 129
- Burkhart B., Lee M.-Y., Murray C. E., Stanimirović S., 2015, *Astrophys. J. Lett.*, 811, L28
- Cesarsky C. J., 1980, *Ann. Rev. Astron. Astrophys.*, 18, 289
- Chandrasekhar S., Fermi E., 1953, *Astrophys. J.*, 118, 113
- Clark S. E., Peek J. E. G., Putman M. E., 2014, *Astrophys. J.*, 789, 82
- Clark S. E., Peek J. E. G., Miville-Deschênes M. A., 2019, *Astrophys. J.*, 874, 171
- Cox D. P., 2005, *Ann. Rev. Astron. Astrophys.*, 43, 337
- Crutcher R. M., 1999, *Astrophys. J.*, 520, 706
- Crutcher R. M., Kemball A. J., 2019, *Frontiers in Astronomy and Space Sciences*, 6, 66
- Crutcher R. M., Wandelt B., Heiles C., Falgarone E., Troland T. H., 2010, *Astrophys. J.*, 725, 466
- Davis Leverett J., Greenstein J. L., 1951, *Astrophys. J.*, 114, 206
- Dickey J. M., Lockman F. J., 1990, *Ann. Rev. Astron. Astrophys.*, 28, 215
- Elmegreen B. G., Scalo J., 2004, *Ann. Rev. Astron. Astrophys.*, 42, 211
- Falgarone E., Troland T. H., Crutcher R. M., Paubert G., 2008, *Astron. Astrophys.*, 487, 247
- Federrath C., 2016, *Journal of Plasma Physics*, 82, 535820601
- Federrath C., Banerjee S., 2015, *Mon. Not. R. Astron. Soc.*, 448, 3297
- Federrath C., Klessen R. S., Schmidt W., 2008, *Astrophys. J. Lett.*, 688, L79
- Federrath C., Chabrier G., Schober J., Banerjee R., Klessen R. S., Schleicher D. R. G., 2011, *Phys. Rev. Lett.*, 107, 114504
- Federrath C., Schober J., Bovino S., Schleicher D. R. G., 2014, *Astrophys. J.*, 797, L19
- Federrath C., Klessen R. S., Iapichino L., Beattie J. R., 2021, *Nature Astronomy*, 5, 365
- Ferrière K. M., 2001, *Reviews of Modern Physics*, 73, 1031
- Ferrière K., 2020, *Plasma Physics and Controlled Fusion*, 62, 014014
- Field G. B., Goldsmith D. W., Habing H. J., 1969, *Astrophys. J. Lett.*, 155, L149
- Gaensler B. M., Madsen G. J., Chatterjee S., Mao S. A., 2008, *PASA*, 25, 184
- Gaensler B. M., et al., 2011, *Nature*, 478, 214
- Gent F. A., Shukurov A., Sarson G. R., Fletcher A., Mantere M. J., 2013, *Mon. Not. R. Astron. Soc.*, 430, L40
- Gent F. A., Mac Low M.-M., Korpi-Lagg M. J., Singh N. K., 2023, *Astrophys. J.*, 943, 176
- HI4PI Collaboration et al., 2016, *Astron. Astrophys.*, 594, A116
- Haffner L. M., Reynolds R. J., Tufte S. L., Madsen G. J., Jaehnig K. P., Percival J. W., 2003, *ApJS*, 149, 405
- Haffner L. M., et al., 2010, in Kothes R., Landecker T. L., Willis A. G., eds, *Astronomical Society of the Pacific Conference Series Vol. 438, The Dynamic Interstellar Medium: A Celebration of the Canadian Galactic Plane Survey*, p. 388 (arXiv:1008.0612), doi:10.48550/arXiv.1008.0612
- Han J. L., Qiao G. J., 1994, *Astron. Astrophys.*, 288, 759
- Han J. L., Manchester R. N., Qiao G. J., 1999, *Mon. Not. R. Astron. Soc.*, 306, 371
- Han J. L., Ferriere K., Manchester R. N., 2004, *Astrophys. J.*, 610, 820
- Han J. L., Manchester R. N., Lyne A. G., Qiao G. J., van Straten W., 2006, *Astrophys. J.*, 642, 868
- Han J. L., Manchester R. N., van Straten W., Demorest P., 2018, *ApJS*, 234, 11
- Harvey-Smith L., Madsen G. J., Gaensler B. M., 2011, *Astrophys. J.*, 736, 83
- Haugen N. E., Brandenburg A., Dobler W., 2004, *Phys. Rev. E*, 70, 016308
- He C.-C., Ricotti M., 2024, arXiv e-prints, p. arXiv:2403.09779
- Heiles C., Troland T. H., 2003a, *ApJS*, 145, 329
- Heiles C., Troland T. H., 2003b, *Astrophys. J.*, 586, 1067
- Heiles C., Troland T. H., 2004, *ApJS*, 151, 271
- Hennebelle P., Falgarone E., 2012, *A&ARv*, 20, 55
- Hewish A., Bell S. J., Pilkington J. D. H., Scott P. F., Collins R. A., 1968, *Nature*, 217, 709
- Hill A. S., Benjamin R. A., Kowal G., Reynolds R. J., Haffner L. M., Lazarian A., 2008, *Astrophys. J.*, 686, 363
- Hollins J. F., Sarson G. R., Shukurov A., Fletcher A., Gent F. A., 2017, *Astrophys. J.*, 850, 4
- Hopkins P. F., 2013, *Mon. Not. R. Astron. Soc.*, 430, 1880
- Hu Z., Wibking B. D., Krumholz M. R., 2023, *Mon. Not. R. Astron. Soc.*, 521, 5604
- Indrani C., Deshpande A. A., 1999, *New Astron.*, 4, 33
- Jiang H., Li H.-b., Fan X., 2020, *Astrophys. J.*, 890, 153
- Kado-Fong E., Kim J.-G., Ostriker E. C., Kim C.-G., 2020, *Astrophys. J.*, 897, 143
- Kalberla P. M. W., Haud U., 2023, *Astron. Astrophys.*, 673, A101
- Kalberla P. M. W., Kerp J., 2009, *Ann. Rev. Astron. Astrophys.*, 47, 27
- Kalberla P. M. W., et al., 2010, *Astron. Astrophys.*, 521, A17
- Kazantsev A. P., 1968, *Soviet Journal of Experimental and Theoretical Physics*, 26, 1031
- Khullar S., Federrath C., Krumholz M. R., Matzner C. D., 2021, *Mon. Not. R. Astron. Soc.*, 507, 4335
- Kim C.-G., Ostriker E. C., 2017, *Astrophys. J.*, 846, 133
- Konstantinou A., Ntormousi E., Tassis K., Pallottini A., 2024, *Astron. Astrophys.*, 686, A8
- Korpi-Lagg M. J., Mac Low M.-M., Gent F. A., 2024, *Living Reviews in Computational Astrophysics*, 10, 3
- Krumholz M. R., Burkhart B., 2016, *Mon. Not. R. Astron. Soc.*, 458, 1671
- Krumholz M. R., Federrath C., 2019, *Frontiers in Astronomy and Space Sciences*, 6, 7
- Krumholz M. R., Burkhart B., Forbes J. C., Crocker R. M., 2018, *Mon. Not. R. Astron. Soc.*, 477, 2716
- Kulsrud R. M., Anderson S. W., 1992, *Astrophys. J.*, 396, 606
- Kulsrud R. M., Cen R., Ostriker J. P., Ryu D., 1997, *Astrophys. J.*, 480, 481
- Larson R. B., 1981, *Mon. Not. R. Astron. Soc.*, 194, 809
- Lazarian A., Pogosyan D., 2000, *Astrophys. J.*, 537, 720
- Lee C. P., Bhat N. D. R., Sokolowski M., Meyers B. W., Magro A., 2024, *PASA*, 41, e080
- Lyne A. G., Smith F. G., 1989, *Mon. Not. R. Astron. Soc.*, 237, 533
- Ma Y. K., et al., 2023, *Mon. Not. R. Astron. Soc.*, 521, 60
- Mac Low M.-M., Klessen R. S., 2004, *Reviews of Modern Physics*, 76, 125
- Mahony E. K., et al., 2022, *Mon. Not. R. Astron. Soc.*, 509, 1690
- Manchester R. N., 1972, *Astrophys. J.*, 172, 43
- Manchester R. N., 1974, *Astrophys. J.*, 188, 637
- Manchester R. N., Hobbs G. B., Teoh A., Hobbs M., 2005, *AJ*, 129, 1993
- Mao S. A., et al., 2017, *Nature Astronomy*, 1, 621
- Marchal A., Miville-Deschênes M.-A., 2021, *Astrophys. J.*, 908, 186
- Martin-Alvarez S., Slyz A., Devriendt J., Gómez-Guijarro C., 2020, *Mon. Not. R. Astron. Soc.*, 495, 4475
- Mathew S. S., Federrath C., Seta A., 2024, *Mon. Not. R. Astron. Soc.*, 521, 60
- McClure-Griffiths N. M., et al., 2009, *ApJS*, 181, 398
- McClure-Griffiths N. M., Stanimirović S., Rybarczyk D. R., 2023, *Ann. Rev. Astron. Astrophys.*, 61, 19
- McKee C. F., Ostriker J. P., 1977, *Astrophys. J.*, 218, 148
- Meneguzzi M., Frisch U., Pouquet A., 1981, *Physical Review Letters*, 47, 1060

- Mestel L., 1966, *Mon. Not. R. Astron. Soc.*, 133, 265
- Mestel L., Spitzer L. J., 1956, *Mon. Not. R. Astron. Soc.*, 116, 503
- Mitra D., Wielebinski R., Kramer M., Jessner A., 2003, *Astron. Astrophys.*, 398, 993
- Miville-Deschênes M. A., Levrier F., Falgarone E., 2003, *Astrophys. J.*, 593, 831
- Mouschovias T. C., 1976a, *Astrophys. J.*, 206, 753
- Mouschovias T. C., 1976b, *Astrophys. J.*, 207, 141
- Murray C. E., et al., 2015, *Astrophys. J.*, 804, 89
- Naab T., Ostriker J. P., 2017, *Ann. Rev. Astron. Astrophys.*, 55, 59
- Newville M., Stensitzki T., Allen D. B., Ingargiola A., 2015, LMFIT: Non-Linear Least-Square Minimization and Curve-Fitting for Python, doi:10.5281/zenodo.11813, <https://doi.org/10.5281/zenodo.11813>
- Nguyen H., Dawson J. R., Lee M.-Y., Murray C. E., Stanimirović S., Heiles C., Miville-Deschênes M. A., Petzler A., 2019, *Astrophys. J.*, 880, 141
- Pakmor R., et al., 2024, *Mon. Not. R. Astron. Soc.*, 528, 2308
- Passot T., Vázquez-Semadeni E., 1998, *Phys. Rev. E*, 58, 4501
- Passot T., Vázquez-Semadeni E., 2003, *Astron. Astrophys.*, 398, 845
- Pattle K., Fissel L., 2019, *Frontiers in Astronomy and Space Sciences*, 6, 15
- Pattle K., Fissel L., Tahani M., Liu T., Ntormousi E., 2023, in Inutsuka S., Aikawa Y., Muto T., Tomida K., Tamura M., eds, *Astronomical Society of the Pacific Conference Series Vol. 534, Protostars and Planets VII*. p. 193 (arXiv:2203.11179), doi:10.48550/arXiv.2203.11179
- Ponnada S. B., et al., 2022, *Mon. Not. R. Astron. Soc.*, 516, 4417
- Rand R. J., Kulkarni S. R., 1989, *Astrophys. J.*, 343, 760
- Rieder M., Teyssier R., 2017, *Mon. Not. R. Astron. Soc.*, 471, 2674
- Rincon F., 2019, *Journal of Plasma Physics*, 85, 205850401
- Ruszkowski M., Pfrommer C., 2023, *A&ARv*, 31, 4
- Ruzmaikin A. A., Sokoloff D. D., Shukurov A. M., eds, 1988, *Magnetic fields of galaxies Astrophysics and Space Science Library Vol. 133*, doi:10.1007/978-94-009-2835-0
- Ruzmaikin A., Sokoloff D., Shukurov A., 1989, *Mon. Not. R. Astron. Soc.*, 241, 1
- Rybarczyk D. R., Wenger T. V., Stanimirović S., 2024, arXiv e-prints, p. arXiv:2409.18190
- Saintonge A., Catinella B., 2022, *Ann. Rev. Astron. Astrophys.*, 60, 319
- Scalo J., Elmegreen B. G., 2004, *Ann. Rev. Astron. Astrophys.*, 42, 275
- Schekochihin A. A., 2022, *Journal of Plasma Physics*, 88, 155880501
- Schekochihin A. A., Cowley S. C., Taylor S. F., Maron J. L., McWilliams J. C., 2004, *Astrophys. J.*, 612, 276
- Schneider N., et al., 2013, *Astrophys. J. Lett.*, 766, L17
- Schober J., Schleicher D., Federrath C., Glover S., Klessen R. S., Banerjee R., 2012, *Astrophys. J.*, 754, 99
- Seta A., Federrath C., 2020, *Mon. Not. R. Astron. Soc.*, 499, 2076
- Seta A., Federrath C., 2021a, *Physical Review Fluids*, 6, 103701
- Seta A., Federrath C., 2021b, *Mon. Not. R. Astron. Soc.*, 502, 2220
- Seta A., Federrath C., 2022, *Mon. Not. R. Astron. Soc.*, 514, 957
- Seta A., Shukurov A., Wood T. S., Bushby P. J., Snodin A. P., 2018, *Mon. Not. R. Astron. Soc.*, 473, 4544
- Seta A., Bushby P. J., Shukurov A., Wood T. S., 2020, *Phys. Rev. Fluids*, 5, 043702
- Seta A., Rodrigues L. F. S., Federrath C., Hales C. A., 2021, *Astrophys. J.*, 907, 2
- Shah H., Seta A., 2021, *Mon. Not. R. Astron. Soc.*, 508, 1371
- Shukurov A., Subramanian K., 2021, *Astrophysical Magnetic Fields: From Galaxies to the Early Universe*. Cambridge Astrophysics, Cambridge University Press
- Skalidis R., Tassis K., 2021, *Astron. Astrophys.*, 647, A186
- Smith F. G., 1968, *Nature*, 218, 325
- Sobey C., et al., 2019, *Mon. Not. R. Astron. Soc.*, 484, 3646
- Squire J., Hopkins P. F., 2017, *Mon. Not. R. Astron. Soc.*, 471, 3753
- Subramanian K., 2016, *Reports on Progress in Physics*, 79, 076901
- Sur S., Subramanian K., 2024, *Mon. Not. R. Astron. Soc.*, 527, 3968
- Sutherland R. S., Dopita M. A., 1993, *ApJS*, 88, 253
- Thompson T. A., Heckman T. M., 2024, *Ann. Rev. Astron. Astrophys.*, 62, 529
- Tritsis A., Panopoulou G. V., Mouschovias T. C., Tassis K., Pavlidou V., 2015, *Mon. Not. R. Astron. Soc.*, 451, 4384
- Troland T. H., Crutcher R. M., 2008, *Astrophys. J.*, 680, 457
- van de Voort F., Bieri R., Pakmor R., Gómez F. A., Grand R. J. J., Marinacci F., 2021, *Mon. Not. R. Astron. Soc.*, 501, 4888
- Vázquez-Semadeni E., 1994, *Astrophys. J.*, 423, 681
- Vázquez-Semadeni E., Hu Y., Xu S., Guerrero-Gamboa R., Lazarian A., 2024, *Mon. Not. R. Astron. Soc.*, 530, 3431
- Veilleux S., Cecil G., Bland-Hawthorn J., 2005, *Ann. Rev. Astron. Astrophys.*, 43, 769
- Wakker B. P., van Woerden H., 1997, *Ann. Rev. Astron. Astrophys.*, 35, 217
- Whitworth D. J., et al., 2024, arXiv e-prints, p. arXiv:2407.18293
- Winkel B., Kerp J., Flöer L., Kalberla P. M. W., Ben Bekhti N., Keller R., Lenz D., 2016, *Astron. Astrophys.*, 585, A41
- Wolfire M. G., Hollenbach D., McKee C. F., Tielens A. G. G. M., Bakes E. L. O., 1995, *Astrophys. J.*, 443, 152
- Wolfire M. G., McKee C. F., Hollenbach D., Tielens A. G. G. M., 2003, *Astrophys. J.*, 587, 278
- Yao J. M., Manchester R. N., Wang N., 2017, *Astrophys. J.*, 835, 29
- Yuen K. H., Hu Y., Lazarian A., Pogosyan D., 2019, arXiv e-prints, p. arXiv:1904.03173
- Yuen K. H., Ho K. W., Lazarian A., 2021, *Astrophys. J.*, 910, 161
- Zel'dovich Ya. B., Ruzmaikin A. A., Molchanov S. A., Sokoloff D. D., 1984, *Journal of Fluid Mechanics*, 144, 1
- Zweibel E. G., 2017, *Physics of Plasmas*, 24, 055402
- de Avillez M. A., Breitschwerdt D., 2005, *Astron. Astrophys.*, 436, 585

APPENDIX A: REPRESENTATIVE H α AND HI SPECTRA

As described in Sec. 2.3, we use H α and HI spectra at pulsar locations to compute the corresponding second moment, m_2 , using Eq. 5 within a local standard of rest velocity range of ± 50 km s $^{-1}$. This allows us to derive the equivalent velocity width and, ultimately, the turbulent velocity along the pulsar sightlines (further detailed in Sec. 2.4).

In Fig. A1, we present representative H α and HI spectra for two pulsars: B1620 – 09 (located away from the Galactic plane) and J1756 – 2251 (closer to the Galactic plane). In both cases, the H α spectra exhibit a single broad peak, likely due to the large velocity channel width of 12 km s $^{-1}$, which may limit sensitivity to small-scale components. In contrast, the HI spectra, with a finer velocity channel width of ~ 1 km s $^{-1}$, reveal significant differences in spectral structure, showing more complex features for pulsars near the Galactic plane. Despite these structural variations, we do not differentiate based on spectral complexity. Instead, we consistently use m_2 to determine the velocity width and subsequently derive the turbulent velocity.

APPENDIX B: $E_{\text{mag}} - E_{\text{kin}}$ RELATIONSHIP FOR ONLY THE ZEEMAN MEASUREMENTS

In the main text, we examined the $E_{\text{mag}} - E_{\text{kin}}$ relation across all three phases of the Milky Way's ISM—ionised, atomic, and molecular (Fig. 2). Among these, the analysis involving the ionised ISM required the most assumptions and approximations (as discussed in Sec. 4). In Fig. B1, we present the results of the power-law fit, $E_{\text{mag}} = C_E E_{\text{kin}}^{\alpha_E}$, derived exclusively from Zeeman measurements for the atomic and molecular phases. The fit suggests a scaling of $E_{\text{mag}} \propto E_{\text{kin}}$ with an exponent α_E closer to 1 than the values obtained in Fig. 2, which includes all three phases. This further reinforces the idea that $E_{\text{mag}} \propto E_{\text{kin}}$ represents a more fundamental physical relation than $B - n$.

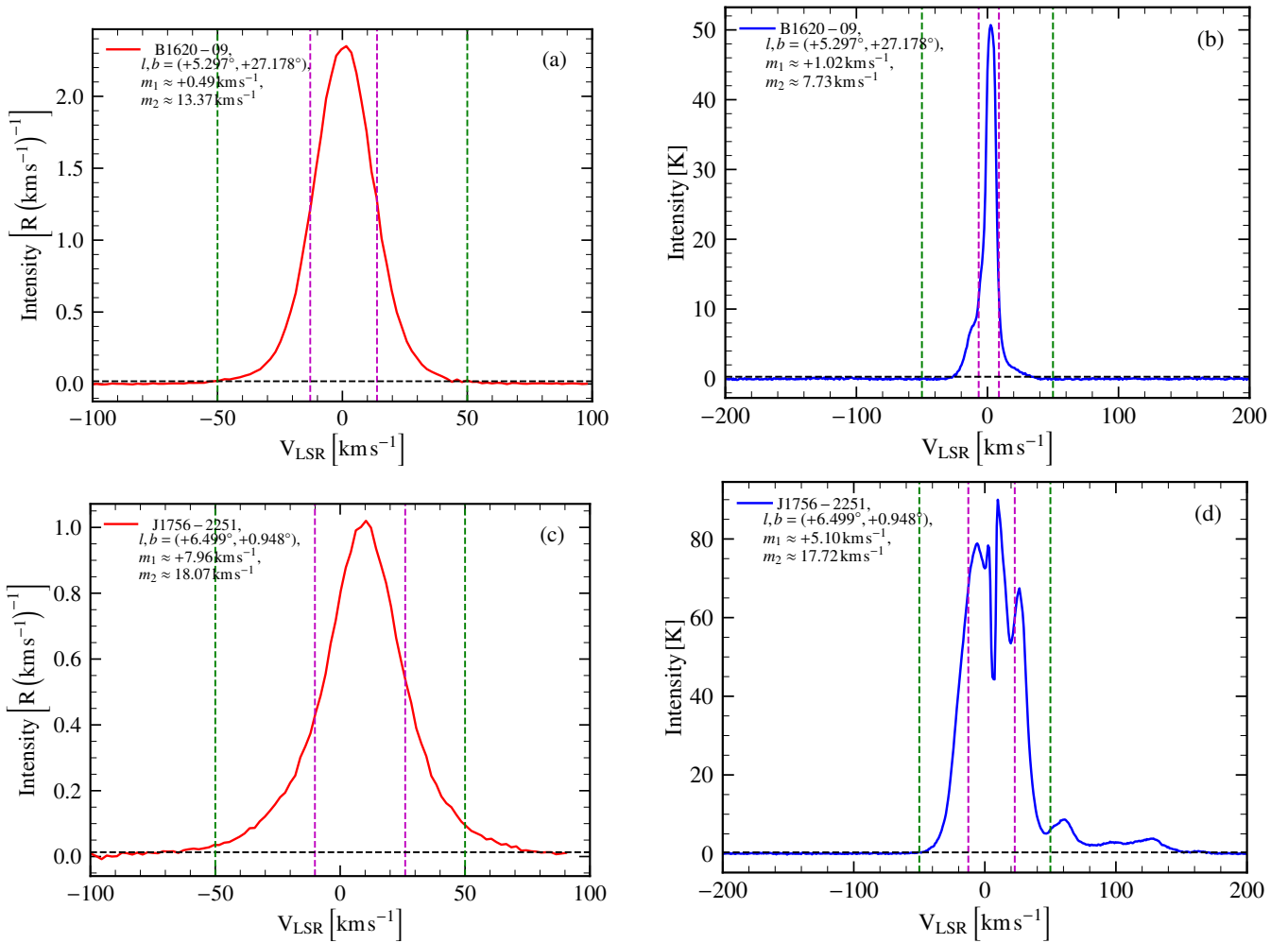


Figure A1. Representative H α (a, c; red) and HI (b, d; blue) spectra for two pulsars: B1620 – 09 (a, b; located away from the Galactic plane) and J1756 – 2251 (c, d; closer to the Galactic plane). The vertical dashed green lines mark the range of Milky Way structures, i.e., the local standard of rest velocities within ± 50 , km, s $^{-1}$, over which the first (m_1) and second (m_2) moments are computed (values given in the legend). The horizontal dashed black line represents three times the noise level, above which the moments are computed (see Sec. 2.3 for numerical values and further details). Finally, the vertical dashed magenta lines indicate the range of m_2 , which is taken as the equivalent velocity width, δv , along the pulsar line of sight, from which the turbulent velocity, δv_{turb} , is derived. For both pulsars, the H α spectra exhibit a single component, possibly due to the large velocity channel width of 12 km s $^{-1}$. In contrast, the HI spectra (with a finer velocity channel width of ~ 1 km s $^{-1}$) reveal more components and greater complexity, particularly for the pulsar located closer to the Galactic plane.

APPENDIX C: $E_{\text{mag}} - E_{\text{kin}}$ RELATIONSHIP INCLUDING MAGNETIC FIELD MEASUREMENTS OBTAINED USING THE DAVIS-CHANDRASEKHAR-FERMI (DCF) METHOD

The Davis-Chandrasekhar-Fermi (DCF) method involves using dispersion in dust polarisation angle to estimate the plane-of-sky magnetic field, B_{pos} (Davis & Greenstein 1951; Chandrasekhar & Fermi 1953). There are a few concerns about the applicability of this method, and some modifications of the classical method are also suggested (see Pattle & Fissel 2019; Skolidis & Tassis 2021; Pattle et al. 2023, for further details). We take the dust polarisation data (n and δv) with B_{pos} obtained using the DCF method from Pattle et al. (2023) ($n_{\text{samp}} = 199$, only those measurements are chosen for which the uncertainties in B_{pos} and δv are available). Then, assuming the Mach number for these measurements, $\mathcal{M}_{\text{DCF}} \approx 1$, we compute δv_{turb} from δv using Eq. 6. Finally, $E_{\text{mag}} = B_{\text{pos}}^2 / 8\pi$ and $E_{\text{kin}} = 0.5 n \delta v_{\text{turb}}^2$ are computed. These are included with those obtained with the pulsars observations and Zeeman measurements and shown in Fig. C1. The entire dataset is fitted with a power-law

function. The exponents of the fit are significantly closer to 1 in comparison to those in Fig. 2, which excludes the DCF values. However, this is expected, as inherently, the DCF method assumes $E_{\text{mag}} = E_{\text{kin}}$ to derive B_{pos} . Thus, this result does not convey significantly new information.

This paper has been typeset from a \LaTeX file prepared by the author.

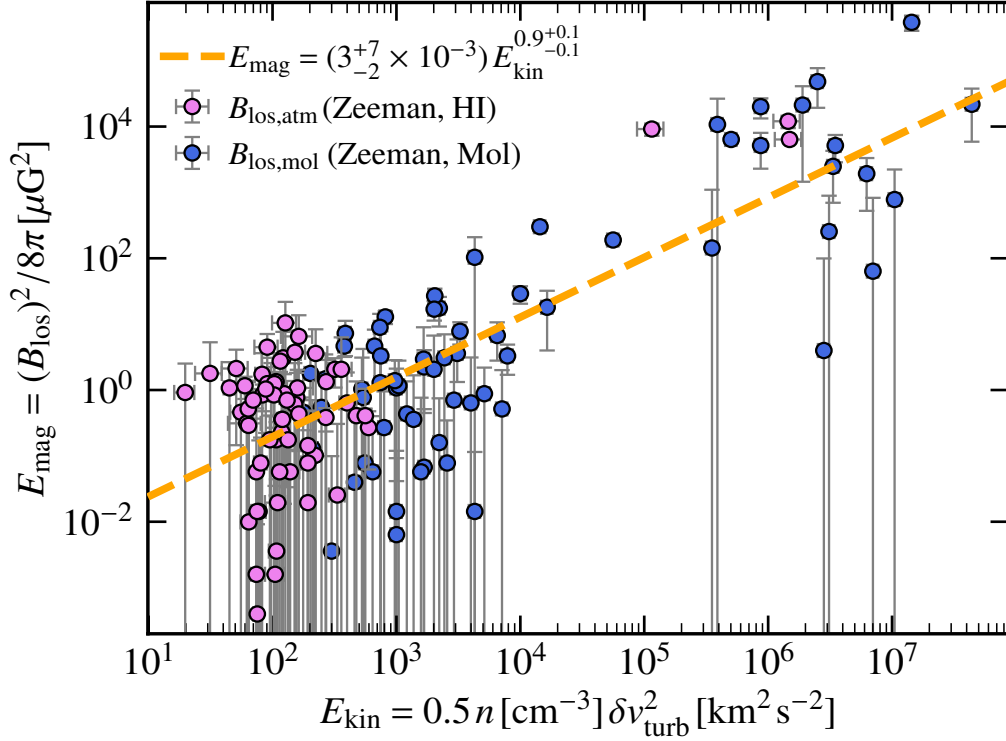


Figure B1. The turbulent kinetic energy density, E_{kin} , and magnetic energy density, E_{mag} , for the atomic (red, probed with Zeeman, HI) and molecular (blue, probed with Zeeman, Mol) phases of the Milky Way’s ISM, along with a power-law fit (dashed orange line). The exponent of the fitted power law is closer to 1 than in Fig. 2, which includes all three phases (ionised, atomic, and molecular), where the analysis involving the ionised phase requires multiple assumptions and approximations (see Sec. 4). This further supports the idea that $E_{\text{mag}} \propto E_{\text{kin}}$ is a more fundamental physical relationship than $B - n$.

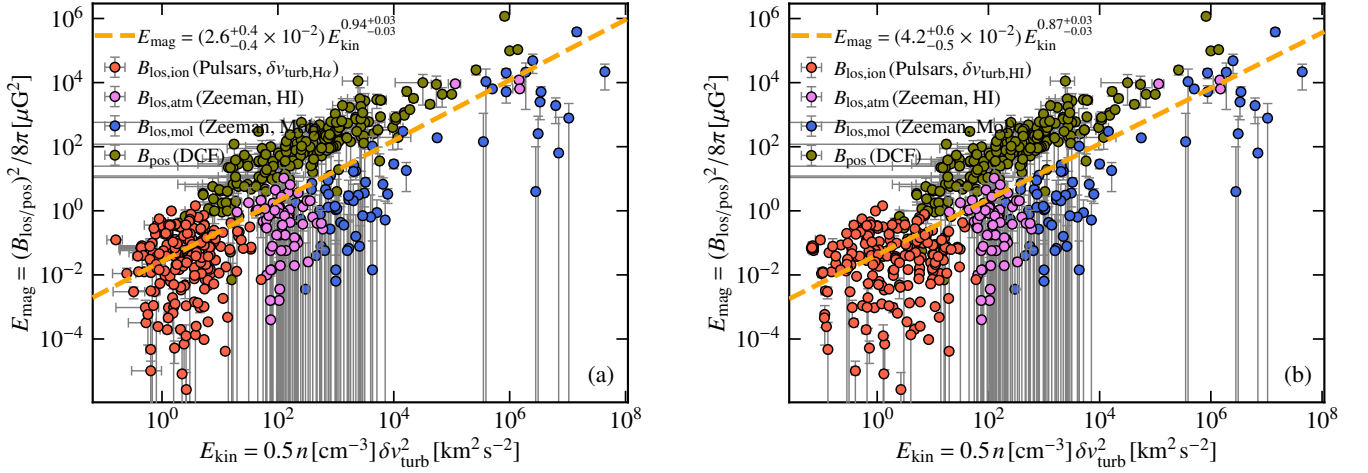


Figure C1. Same as Fig. 2 but now also including the plane-of-sky magnetic field measurements, B_{pos} , obtained using the Davis-Chandrasekhar-Fermi (DCF) method, data taken from [Pattle et al. 2023](#). The exponent of the power-law fit for both cases is closer to 1 in comparison to those in Fig. 2, further emphasising the $E_{\text{mag}} - E_{\text{kin}}$ relation. However, the DCF method intrinsically assumes $E_{\text{mag}} = E_{\text{kin}}$ to derive B_{pos} and thus this is expected.